

## QUANTITATIVE ANALYSIS OF SUBMARINE-FLOW DEPOSIT SHAPE IN THE MARNOSO-ARENACEA FORMATION: WHAT IS THE SIGNATURE OF HINDERED SETTLING FROM DENSE NEAR-BED LAYERS?

GIUSEPPE MALGESINI,<sup>1,2</sup> PETER J. TALLING,<sup>1</sup> ANDREW J. HOGG,<sup>4</sup> DOMINIC ARMITAGE,<sup>3</sup> ALEX GOATER,<sup>4</sup> AND FABRIZIO FELLETTI<sup>2</sup>

<sup>1</sup>National Oceanography Centre, European Way, Southampton, SO14 3ZH, U.K.

<sup>2</sup>Università degli Studi di Milano, Dipartimento di Scienze della Terra, Via Mangiagalli 34, 20133-Milano, Italy

<sup>3</sup>ConocoPhillips, Sedimentology and Stratigraphy, Houston, Texas 77079, U.S.A.

<sup>4</sup>Centre for Environmental & Geophysical Flows, School of Mathematics, University of Bristol, University Walk, Bristol BS8 1TW, U.K.  
e-mail: [giuseppe.malgisini@gmail.com](mailto:giuseppe.malgisini@gmail.com)

**ABSTRACT:** Submarine sediment density flows are one of the volumetrically most important processes for sediment transport across Earth. The sediment concentration of flows that reach the deep ocean has never been measured directly, and understanding these long-runout flows remains a major challenge. The Miocene Marnoso-Arenacea Formation in the Italian Apennines is the only ancient sequence where individual submarine sediment-density-flow deposits (single beds) have been mapped out for more than 100 km down-flow. Here we document the external shape and internal architecture of thirty-two individual beds that record flow evolution and can be compared to deposit shapes in mathematical or experimental models. The large number of beds allows modes of flow behavior to be identified. Larger-volume turbidites are typically dominated by massive ( $T_A$ ) or planar-laminated ( $T_B$ ) sandstone intervals that have a broad thickness maximum. This shape is important because it suggests that massive and planar laminated sandstones record hindered settling from dense near-bed layers, which have high (> 10% by volume) sediment concentrations. Previously, some authors have inferred that planar-laminated sandstones ( $T_B$ ) are deposited mainly by dilute flows. The position of the broad thickness maximum moves basinward as the volume of sand in the flow increases. This is consistent with mathematical modeling that suggests the position of the thickness maximum depends on flow thickness, flow speed, and sediment settling velocity, as well as sediment concentration, variations in seawater entrainment rate, and local changes in seafloor gradient. Smaller-volume turbidite sandstone intervals are finer grained and dominated by ripple cross-lamination ( $T_C$ ) and have a near exponential decay in thickness that is consistent with deposition from a dilute sediment suspension. The rate of near exponential thinning is controlled by sandstone volume. In contrast, turbidite mudstone intervals show an approximately linear increase in thickness with distance. Flows that entered the basin in opposite directions produced turbidite mudstone intervals that thicken towards the same location, indicating that muddy turbidity currents can drain back over long distances to basinal lows.

### INTRODUCTION

There are remarkably few direct measurements from active submarine sediment-laden density flows (Xu 2011; Puig et al. 2014; Talling et al. 2014; Talling 2014), even though they dominate sediment fluxes across large areas of the planet. For instance, the sediment concentration of flows that reach the deep ocean (beyond the base of the continental slope) has never been measured directly, and it is uncertain whether they contain dense near-bed layers. This means that much of our understanding of such flows must be pieced together from studies of their deposits.

Here we analyze the shape of individual ancient flow deposits (single beds) in order to understand how submarine flows evolve. In particular, we wish to understand whether deposit shape provides evidence for (or against) deposition from dense near-bed layers characterized by hindered settling. Very few studies have documented the shape of turbidite beds by correlating individual flow deposits for long (> 100 km) distances (Amy and Talling 2006; their table 1). This is because turbidite deposits are commonly eroded by subsequent flows, causing local bed truncation and amalgamation (Enos 1969), and because suitable marker beds that allow

correlation are rare. The Miocene Marnoso-Arenacea Formation, in the northern Italian Apennines, provides the most extensive correlation of individual flow deposits (single beds) yet documented for any ancient turbidite sequence (Ricci Lucchi and Valmori 1980; Amy and Talling 2006; Talling et al. 2007a, 2012, 2013a, 2013b; Muzzi Magalhaes and Tinterri 2011), although longer-distance (up to 2,000 km) correlations have been made using relatively short (< 10 m) cores from the modern sea floor (Frenz et al. 2008; Talling et al. 2007c; Wynn et al. 2010). The Marnoso-Arenacea Formation has an advantage over modern sea-floor cores in that many tens of beds can be studied, allowing modes of down-flow evolution be better constrained. However, changes in sea-floor gradient are more poorly constrained for ancient rock sequences. We therefore discuss the extent to which it is possible to determine how variable seafloor gradients affected these ancient bed geometries.

This study is novel because of the large number of beds described, which aids recognition of underlying first-order trends in bed shape (cf. Tinterri et al. 2003; Falcini et al. 2009, and others). Previous analyses of bed shape by Talling et al. (2007a) and Sumner et al. (2012) were

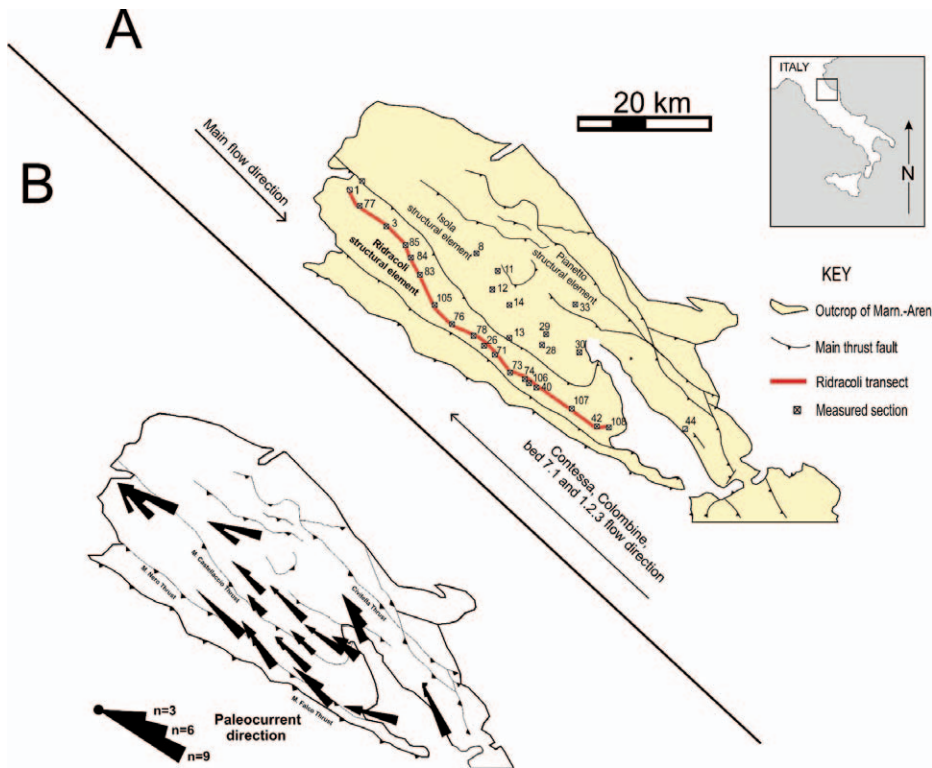


FIG. 1.—A) Location map showing the northern part of the outcrop of the Marnoso-Arenacea Formation. The figure shows the position of measured sections. It also shows the transect along the Ridracoli Element along which beds in the below-Contessa interval have been correlated (red line). Sections are numbered as for Amy and Talling (2006) and Talling et al. (20012a). B) Paleocurrent directions measured from flutes and grooves on the base of the beds in the below-Contessa interval. Modified from Talling et al. (2013a).

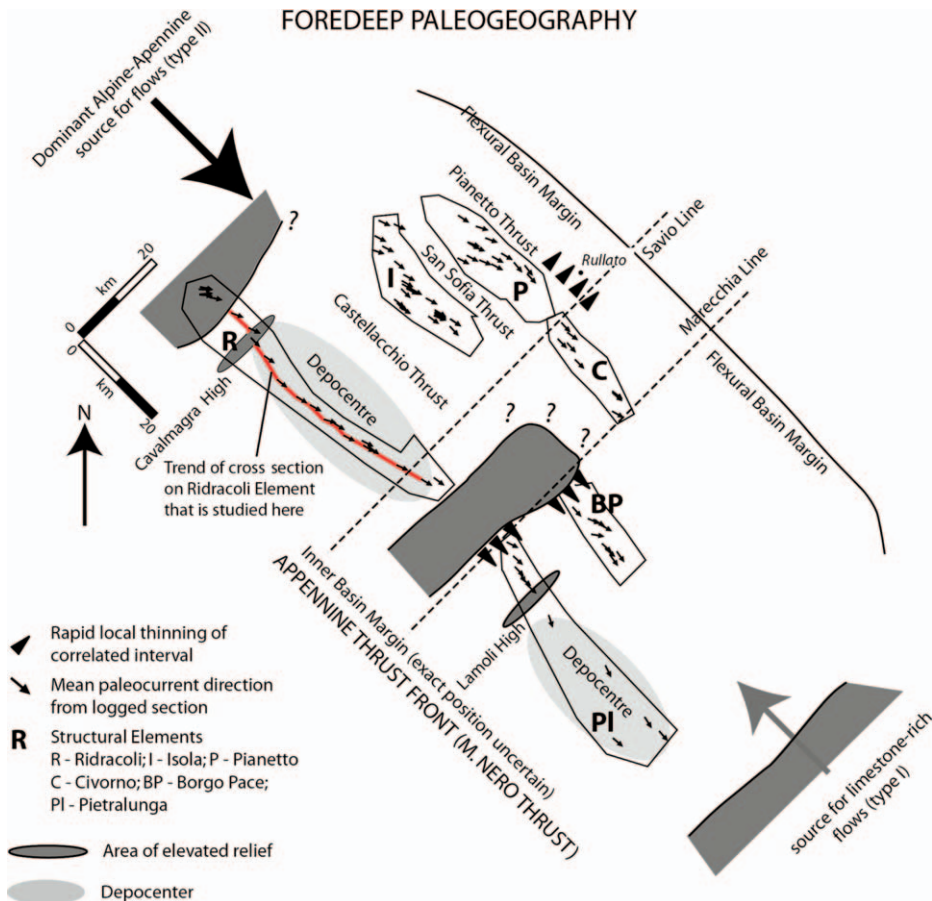


FIG. 2.—Paleogeographic reconstruction of the Marnoso-Arenacea Formation “inner” foredeep basin at the time of deposition for the above Contessa interval. Structural elements have been repositioned to reflect structural reconstructions that suggest that the basin was originally twice as wide (Ricci Lucchi and Valmori 1980). The mean paleocurrent direction for each logged section is shown. From Talling et al. (2007a).

TABLE 1.—Cross-sectional area of different lithofacies, and the sand/mud ratio for each bed, in the Ridracoli thrust sheet.

Bed	Prov.	Area (m <sup>2</sup> )							
		Total	Sand	Mud	T <sub>a-b</sub>	T <sub>c-d</sub>	Dcs	Dm	S/M
Col.	SE	86569	12411	74158	0	12411	0	0	0.17
8.1.2	NW	8807	665	8142	0	665	0	0	0.08
8	NW	41029	20685	20344	16343	4341	0	0	1.02
7.9	NW	24122	11676	12446	1909	9767	0	0	0.94
7.1	SE	12862	471	12391	0	471	0	0	0.04
7	NW	59198	21188	38010	16000	1936	0	3251	0.56
6	NW	90795	51923	38872	30480	11995	0	9448	1.34
5.3	NW	16730	9399	7331	0	9399	0	0	1.28
5.1	NW	42840	28988	13852	12446	5425	11116	0	2.09
5	NW	76006	49987	26019	36284	5173	0	8529	1.92
4.1	NW	15929	6296	9633	0	6296	0	0	0.65
4	NW	94866	57319	37547	40800	16519	0	0	1.53
3	NW	73187	51569	21618	32888	5262	0	13418	2.39
2.5	NW	26633	12084	14549	7838	1382	0	2863	0.83
2	NW	66750	51944	14806	28220	23723	0	0	3.51
1.5	NW	10651	3018	7633	0	3018	0	0	0.39
1.2.3	SE	32135	6894	25241	0	6894	0	0	0.27
1	NW	40108	21359	18749	14056	2585	0	4717	1.14
0	NW	61173	49860	11313	23994	12874	12991	0	4.41
-2	NW	65892	49531	16361	35011	14519	0	0	3.01
-5	NW	16716	8081	8635	0	8081	0	0	0.94
-6	NW	67280	57621	9659	43820	5769	8031	0	5.97
-7	NW	67448	52312	15136	44107	6691	0	1512	3.46
-8	NW	47115	38737	8378	0	6493	32243	0	4.62
-9	NW	10173	3609	6564	0	2652	2080	0	0.55
-10	NW	56272	40497	15775	33593	6903	0	0	2.57
-11	NW	42405	35044	7361	30105	869	0	4069	4.76
-12	NW	10729	5909	4820	0	5909	0	0	1.23
-13	NW	24014	15315	8699	3556	5062	6696	0	1.76
-14	NW	76375	65829	10546	49207	6949	9672	0	6.24
-15	NW	39218	33436	5782	29977	3458	0	0	5.78
-16	NW	68557	57351	11206	44323	4512	0	8515	5.12

qualitative, rather than the quantitative analysis that is presented here. This contribution then presents novel results from mathematical models of the flows that provide key insights into how deposit shape is related to sediment concentration at the base of the flow. In particular, it assesses whether bed shape provides a record of hindered settling, and hence relatively dense near-bed concentrations. This comparison helps to understand the origin of different types of sandstone, especially planar-

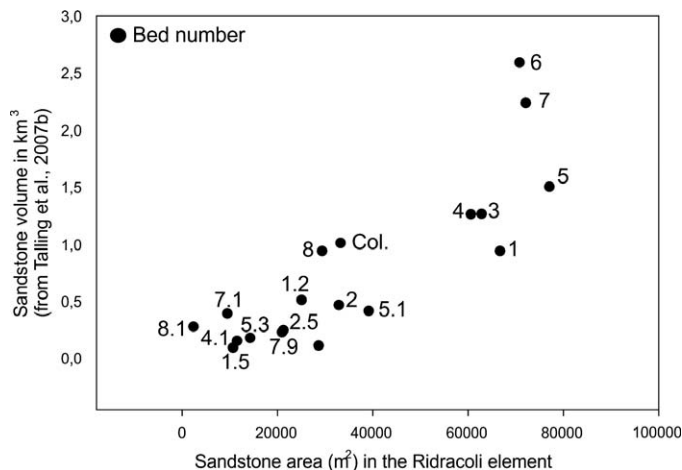


FIG. 3.—Comparison between the sandstone volumes estimated by Talling et al. (2007b) using 109 locations on seven thrust sheets (Fig. 1) and the cross sectional areas calculated for each sandstone interval in the Ridracoli thrust sheet (Fig. 1). Data are from beds in the above-Contessa stratigraphic interval.

laminated sandstone comprising the T<sub>B</sub> division of Bouma (1962). Debate surrounds whether planar laminated T<sub>B</sub> intervals are formed by flows with high or low near-bed concentrations, inasmuch as both dilute and dense flows can form planar lamination in laboratory experiments (Kuenen 1966; Best and Bridge 1992; Leclair and Arnott 2005; Sumner et al. 2008). More generally, it is hoped that future studies will compare the field dataset presented here to the deposits of laboratory and mathematical models in order to better understand flow processes, issues of scaling in laboratory flows, and the validity of assumptions used to formulate numerical models.

#### Aims

Initial analysis of field observations aims to determine (i) whether beds or depositional intervals (e.g., Bouma-sequence intervals T<sub>A-10-E</sub>) within beds display consistent shapes, and what these shapes are, (ii) how bed or interval shape changes with increasing flow volume or grain size, and (iii) how bed architecture most likely records flow processes. The aim of subsequent numerical modeling is to investigate how sandstone interval shape depends on the sediment concentration within the flow. Numerical modeling tests the specific hypothesis that massive (T<sub>A</sub>) and planar-laminated (T<sub>B</sub>) sandstone intervals are deposited by flows with dense near-bed layers from which hindered settling occurs, whilst thinner sandstones dominated by cross-laminated (T<sub>C</sub>) intervals are deposited by dilute flows.

#### GEOLOGICAL BACKGROUND

The beds studied in the Marnoso-Arenacea Formation were deposited within a nonchannelized basin plain, and are separated by intervening

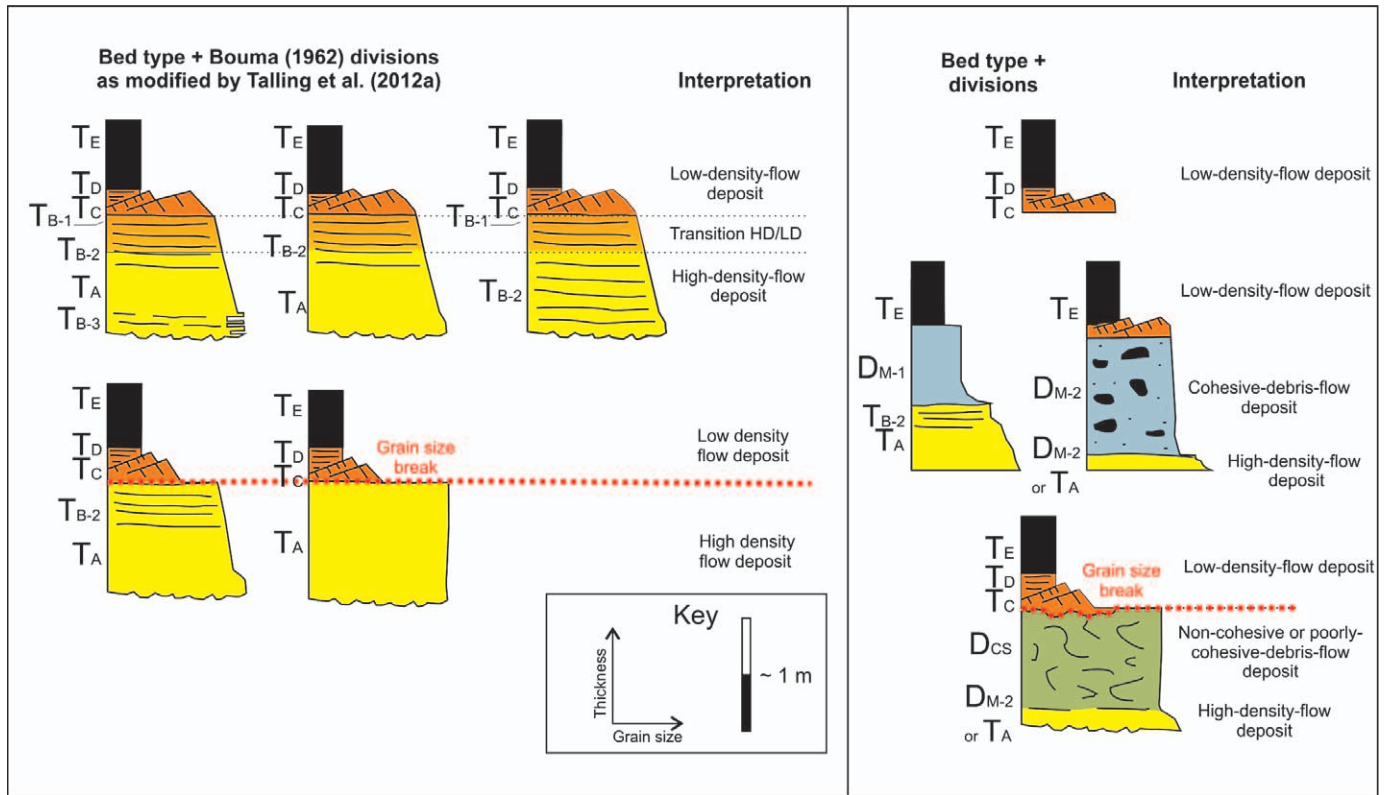


FIG. 4.—Generalized graphic sedimentary logs that summarize the deposits produced by different types of submarine flow. Depositional intervals and the corresponding Bouma (1962) division, as modified by Talling et al. (2012a), are shown. The inferred depositional process is indicated for each type of interval.

hemipelagic mud (Ricci-Lucchi and Valmori 1980; Amy and Talling 2006; Talling et al. 2007a, 2007b, 2012; Sumner et al. 2012; Dall’Olio et al. 2013). Megaturbidites act as marker beds, allowing intervening beds to be correlated between more than one hundred sections across the whole basin. This topographically simple basin plain setting has produced a “layer cake” stratigraphy with virtually no bed amalgamation and little or no evidence for erosion or flow reflection (except in the megaturbidites; Talling et al. 2007b). It was thought initially by the authors that this topographically simple basin-plain setting would produce simple bed geometries (i.e., those lacking the confounding effects of flow reflection, deflection, or erosion due to steeper slopes) that could be easily compared to the results of numerical models. However, despite the simple topographic setting, the beds are complex. They often record multiple flow types within a single overall event, with lateral or down-flow transitions between flow types (Amy and Talling 2006; Talling et al. 2007a, 2007b, 2012, 2013a, 2013b; Sumner et al. 2012). Some of these flow transitions have now been recognized in hybrid beds from many other locations worldwide (Haughton et al. 2003, 2009; Talling et al. 2004, 2010, 2012, 2013a), whilst other types of flow transformation (e.g., those involving clean-sand debris flows; Talling et al. 2013b) are more contentious.

**METHODOLOGY**

**Bed Correlations**

Detailed bed correlation figures are presented in previous papers. Amy and Talling (2006), Talling et al. (2007a, 2007b, 2013a, 2013b) and Sumner et al. (2012) documented the geometry of 56 beds between the Contessa megabed and the first overlying Colombine marker (“above-Contessa interval” in this article). Further work (Talling et al. 2013a) mapped an additional 13 beds located immediately below the Contessa

megabed (termed the “below-Contessa interval”). This contribution analyzes the shape of 32 beds in a 60-km-long cross section along the Ridracoli structural element, whose trend is subparallel to the dominant paleo-flow direction (Figs. 1, 2; Amy and Talling 2006; Talling et al. 2007a, 2007b, 2013b).

Thick (> 40 cm) beds in the above Contessa interval were named bed 0 to bed 8. Beds located between key beds are numbered according to their position above each key bed. Beds in the below Contessa interval are numbered sequentially from -1 to -20, with our Bed -20 also being bed A-20 in the scheme of Ricci Lucchi and Valmori (1980).

**Differential Compaction**

It is assumed herein that uniform compaction affected sandstone intervals, and their shape is not otherwise distorted significantly. The maximum burial depth of Marnoso-Arenacea Formation outcrops varies from ~ 5 to ~ 2.5 km across the foredeep basin (Zattin et al. 2002). This is likely to cause variations in the original sandstone thickness of approximately 16% (Amy and Talling 2006). However, burial depths show less variation along transects used to define bed shape that are orientated parallel to the basin axis (Zattin et al. 2002, their fig. 16). Mudstone intervals will have been compacted to a greater degree than sandstone intervals (Amy and Talling 2006).

**Field Constraints on Seafloor Topography**

We now outline available field constraints on basin topography, because changes in seafloor gradient can strongly effect deposition and erosion from submarine flows (e.g., Talling et al. 2007a; Wynn et al. 2010; Stevenson et al. 2013). We later discuss how changes in gradient can be identified in these bed geometries, and have affected bed geometry.

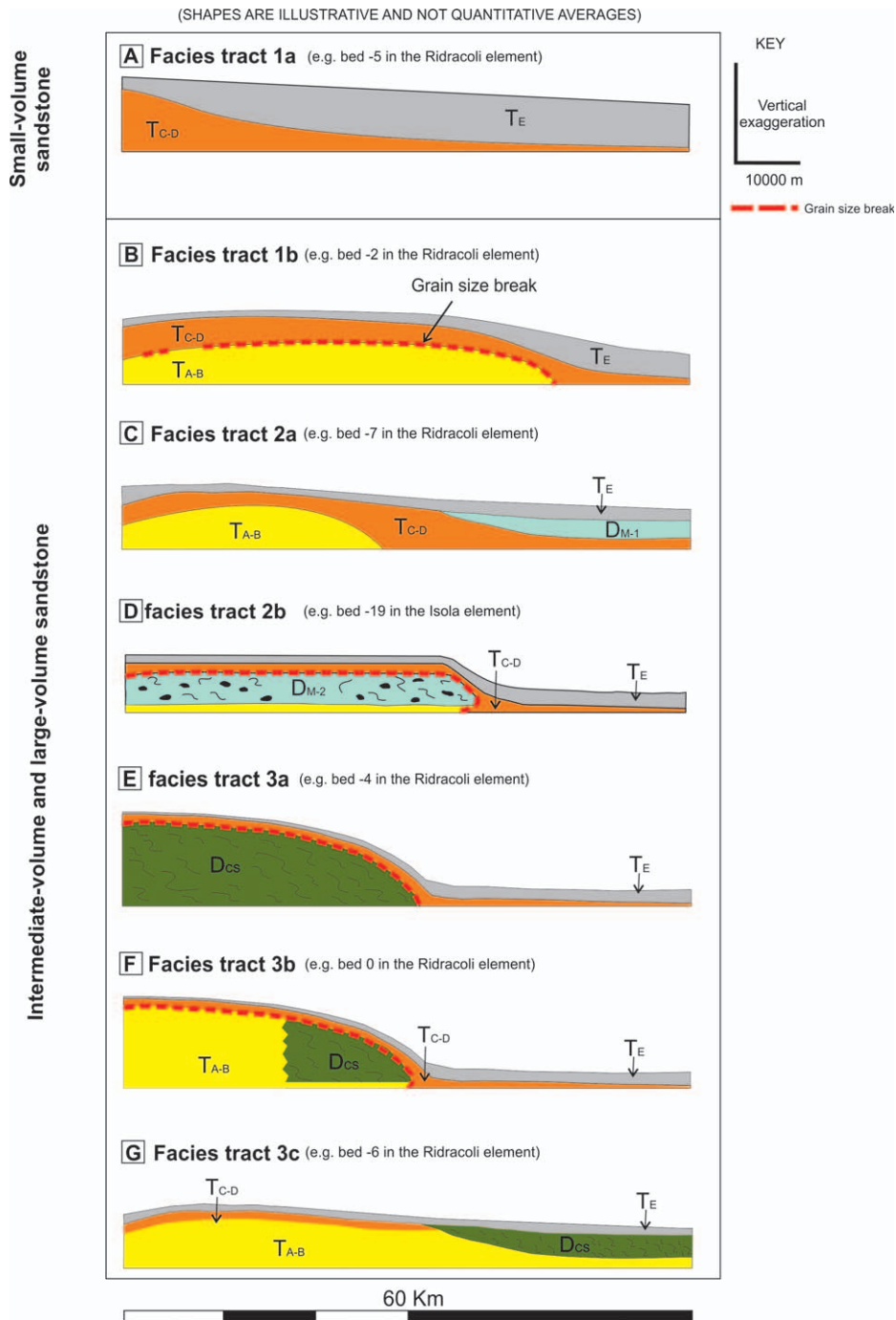
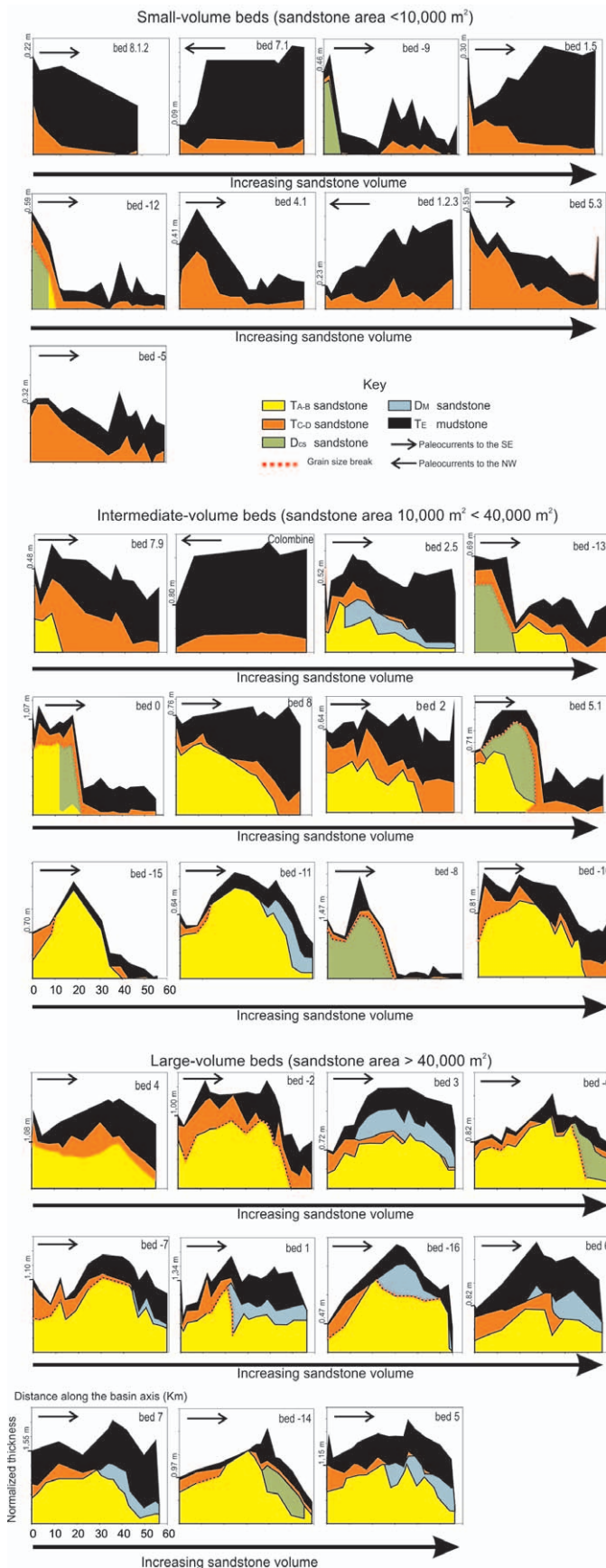


FIG. 5.—Generalized facies tracts observed for correlated beds in the Marnoso-Arenacea Formation. Bed-thickness variations are illustrative, not quantitative changes. From Talling et al. (2013a).

The beds studied here were deposited in a relatively flat basin plain, as shown by the ability of the flows to transverse the area in opposing directions, the complete absence of channelization, and the continuous “layer-cake” bed geometry (Ricci Lucchi and Valmori 1980; Amy and Talling 2006; Talling et al. 2007a, 2013a, 2013b). Modern basin plains with this type of “layer-cake” stratigraphy tend to have sea floor gradients of  $< 0.05^\circ$  (Talling et al. 2007c), suggesting similarly low gradients for the Marnoso-Arenacea basin plain. However, the Marnoso-Arenacea basin plain was not entirely flat when these beds were deposited. Three subtle intrabasinal highs (Verghereto, Cavalmagra, and Lamoli highs, Fig. 2) were previously inferred from isopachs of the above-Contessa and below-Contessa intervals, from consistent fluctua-

tions in mud or sand thickness within multiple consecutive beds, and from the local termination of some thin beds (Talling et al. 2007a). The Verghereto high had a greater bathymetric relief than the Cavalmagra and Lamoli highs (Talling et al. 2007a). The flows were able to overtop the highs without significant deflection (Figs. 1, 2), and their relief is inferred to be substantially less than the thickness of the flows (Talling et al. 2007a). It is also significant that beds are continuous across two of these highs, because small changes in gradient can cause changes from depositional to nondepositional flows in modern basin-plain systems (Talling et al. 2007c; Wynn et al. 2010; Stevenson et al. 2013). Changes in gradient associated with the Cavalmagra and Lamoli Highs were insufficient to cause flows to become nondepositional, although a hiatus



in deposition may characterize the Verghereto High (Talling et al. 2007a). The available paleocurrent data suggest little or no reflection of the sandy component of these flows (Figs. 1, 2; Talling et al. 2007a, 2012, 2013a, 2013b), although mud reflected and ponded in the southern part of the basin, suggesting that this area was the lowest point in the basin. The correlated beds thin towards the flexural basin margin, as expected for a foreland basin (Figs. 1, 2; Amy and Talling 2006), suggesting that there was a lateral gradient within the basin.

**Bed Volumes and Cross-Sectional Areas**

The cross-sectional area of sandstone and mudstone intervals was estimated for each bed for the cross section along the Ridracoli structural element (Fig. 1), instead of the bed volume. This avoids uncertainties in volume estimates due to the poorly constrained basin width. The area of each bed, and lithofacies within each bed, is presented in Table 1. It is reasonable to assume that beds with larger cross-sectional area in the Ridracoli Element correspond generally to larger-volume beds in the wider basin (Fig. 2), as confirmed by a comparison between the cross-sectional area calculated in this study and the total sandstone volume obtained by Talling et al. (2007b; Fig. 3).

**Depositional Processes from Observations at a Single Outcrop**

The most likely origin of individual lithofacies has been described previously (see Table 1 of Talling et al. 2013b), and therefore it is only summarized briefly here.

**Massive Sandstone (T<sub>A</sub>)**

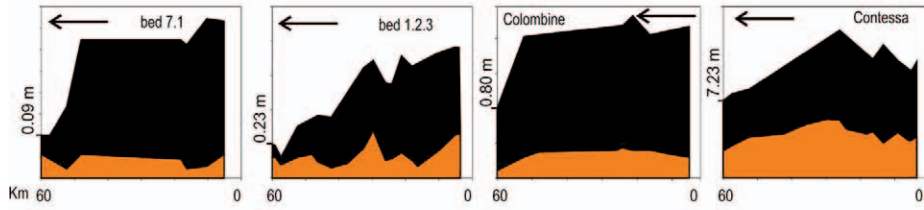
Clean (mud-poor) massive sandstone can form in a number of ways from flows with high near-bed sediment concentrations, by direct sedimentation or collapse of discrete near-bed layers, as summarized by Talling et al. (2012; their fig. 15). Massive turbidite sandstone records evidence of progressive layer-by-layer deposition in the form of vertical grading, discrete horizons of mud clasts, or a gradually tapering deposit shape (see Talling et al. 2012).

**Mud-Rich Cohesive Debrite Sandstone (D<sub>M</sub>)**

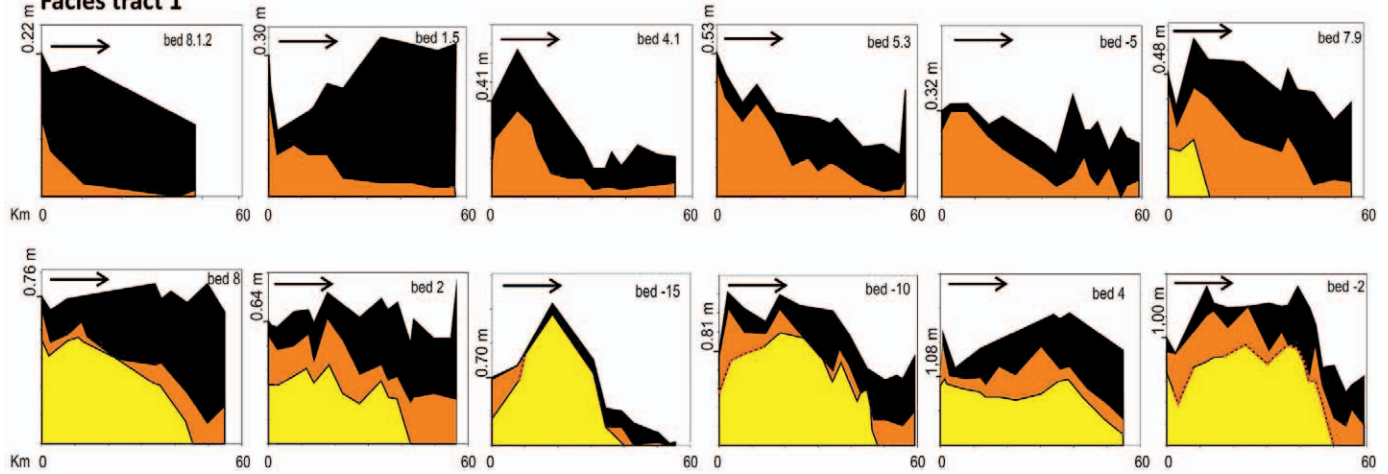
Cohesive debris flows deposit mud-rich and predominantly ungraded sandstone that records evidence of en-masse deposition. A continuum of increasing cohesive-debris-flow-strength produces variations in debrite character (as summarized by Talling et al. 2012, 2013a). Low-strength debris flows produce clast-poor debrite sandstones, which tend to grade laterally into silt along the flow path. They may resemble fluid-mud layers, and can form through local flow transformation and turbulence collapse (Sumner et al. 2009; Baas et al. 2011). Higher-strength debrites contain larger clasts and tend to pinch out abruptly. These debris flows can run out for tens of kilometers across the basin plain from an external source (Talling et al. 2013b).

FIG. 6.—Diagrams illustrating the lateral changes in thickness and internal facies architecture in the 32 turbidite beds from the above-Contessa and below-Contessa intervals, along the Ridracoli Element in a direction subparallel to paleoflow. Beds are ordered with increasing sandstone cross sectional area. As shown by arrows, flows traversed this basin floor in one of two opposing directions. Bed thickness has been normalized. This was done by dividing each thickness by the thickness of each bed at the most proximal section at km 0 (Coniale-1 section, see Fig. 1A). The total bed thickness at km 0 (Coniale-1) is indicated for each bed. Note that the vertical exaggeration is very large, typically about 1:30,000. The key shows the facies types used to subdivide each bed, whose rationale is discussed in the text.

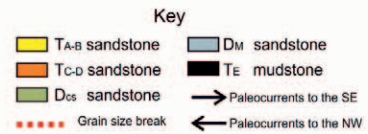
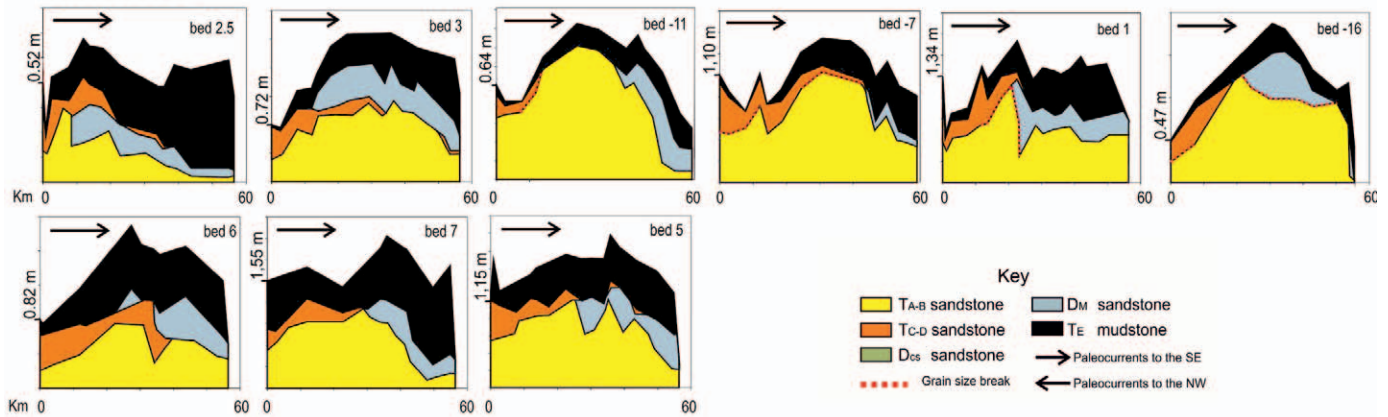
**Beds from the South East**



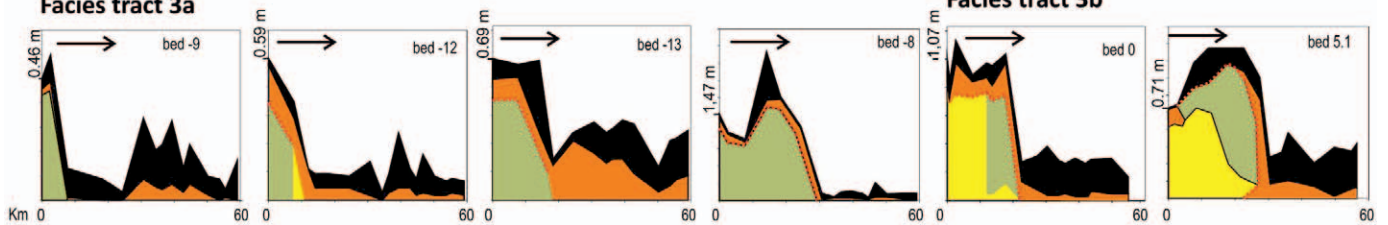
**Facies tract 1**



**Facies tract 2a**

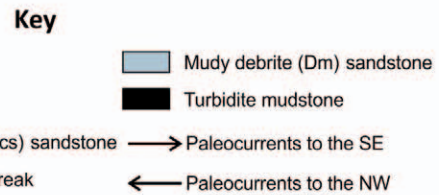
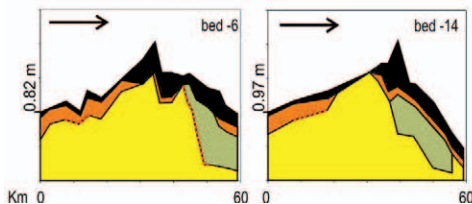


**Facies tract 3a**



**Facies tract 3b**

**Facies tract 3c**



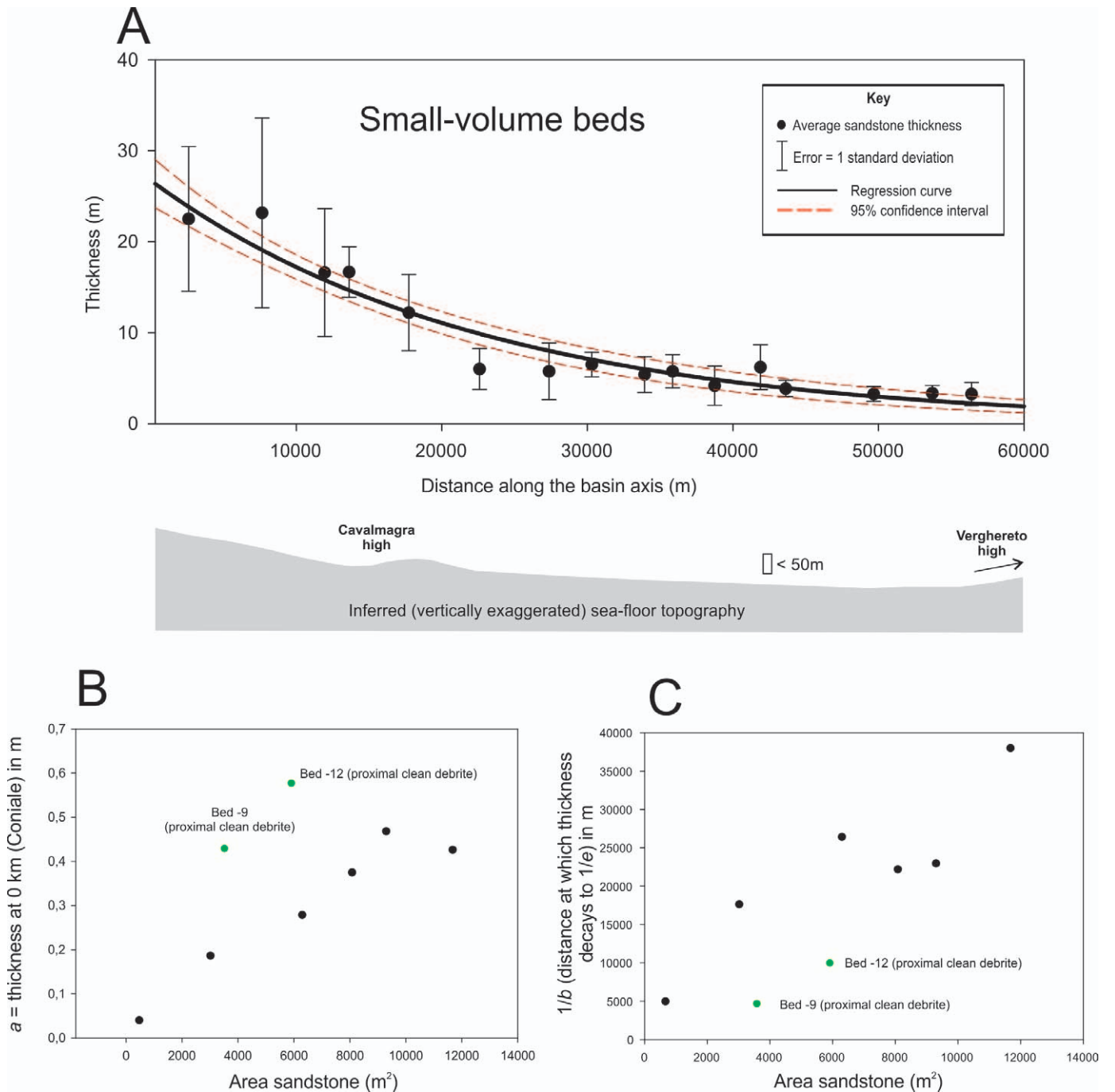


FIG. 8.—Sandstone interval shape in small-volume beds along the Ridracoli thrust sheet (Fig. 1). **A**) Regression curve describing the lateral thickness variations in the average thickness of sandstone intervals in small-volume beds, which are shown in Figure 5. The 95% confidence limit and the standard deviation of sandstone thickness in each section are shown. The regression coefficients are shown in Table 2. **B**) Sandstone thickness in each of the nine beds at the Coniale section (corresponding to the “ $a$ ” parameter in the regression curve) plotted against the calculated sandstone cross-sectional area. Maximum sandstone thickness plotted against the calculated sandstone cross-sectional area. **C**) Distance over which thickness decays to  $1/e$  (37%) of its original value, which is equivalent to  $1/b$  in the best-fit line. This distance is also named the *e-fold length*, and here it is plotted against the cross-sectional sandstone area of small-volume beds. **D**) Regression curve describing the exponential thinning of sandstone intervals in small-volume beds with provenance from the northwest.

←

FIG. 7.—Diagrams illustrating the lateral changes in thickness and internal facies architecture in the 32 turbidite beds from the above-Contessa and below-Contessa intervals, along the Ridracoli Element in a direction subparallel to paleoflow. Beds are subdivided according to the downflow facies architecture (facies tracts). As shown by arrows, flows traversed this basin floor in one of two opposing directions. Bed thickness has been normalized. This was done by dividing each thickness by the thickness of each bed at the most proximal section at km 0 (Coniale 1 section, see Fig. 1A). The total bed thickness at km 0 (Coniale) is indicated for each bed. Note that the vertical exaggeration is very large, typically about 1:30,000. The key shows the facies types used to subdivide each bed, whose rationale is discussed in the text.

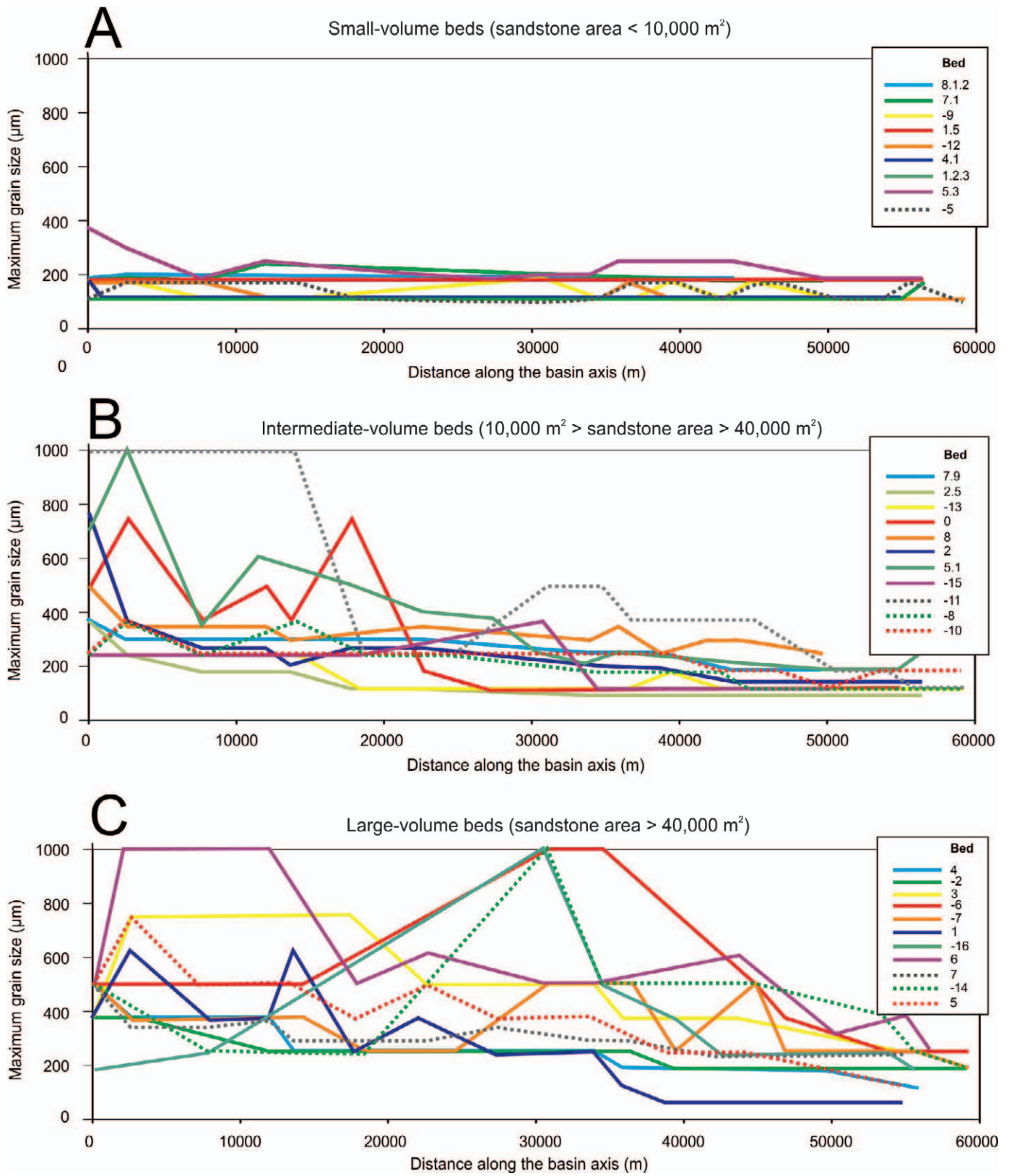


FIG. 9.—Variation of the maximum grain-size measured using a grain size comparator card in the field, for **A**) small-volume beds, **B**) intermediate-volume beds, and **C**) large-volume beds. Note that these values typically correspond to approximately the coarsest 95% percentile of grain-size distributions measured from long axes of grains in thin sections (Talling et al. 2004).

### Clean Debrite Sandstone ( $D_{CS}$ )

The fraction of mud in the matrix of these clean sandstone ( $D_{CS}$ ) debrites is similar to that in turbidite sandstone intervals (Talling et al. 2013b), and significantly lower than the mud-matrix fraction in mud-rich cohesive debrites (Talling et al. 2013). The ability of clean-sand debrite flows to transport sediment into the deep ocean has previously been contentious, and the transport processes are as yet poorly understood. However, work in the Marnoso-Arenacea Formation suggests that massive clean sandstone can sometimes be deposited in an en-masse fashion by debris flow. Such clean sandy debrites often have a subtle but distinctive swirly fabric, comprising contorted areas of coarser or better-sorted grains that record pervasive liquefaction (Talling et al. 2012, 2013a). Deposition by debris flow is consistent with the observed relatively abrupt lateral pinch-out of such deposits (see Talling et al. 2012, 2013a). As with mud-rich cohesive debrites several different facies tracts are observed for clean sand debrites. The clean sand debrites could also result from late-stage turbulence collapse, as for mud-rich debrites, and variations in  $D_{CS}$  facies tract could also be linked to changes in debris-flow yield strength (Talling et al. 2013b).

### Planar-Laminated Sandstone ( $T_B$ )

Laboratory experiments show that laminated sandstone intervals ( $T_B$ ) can potentially be formed by both low-density and high-density turbidity currents (Talling et al. 2012). Two distinct types of planar-laminated sandstone occur in the Marnoso-Arenacea Formation with finer-scale ( $T_{B-2}$  or  $T_{B-3}$ ) or thicker “stepped” planar ( $T_{B-1}$ ) lamination (Table 1; Sumner et al. 2012; Talling et al. 2012). Fine scale planar lamination can form incrementally by migration of low-amplitude bed waves beneath dilute flows ( $T_{B-3}$ ; Best and Bridge 1992), or by repeated collapse of traction carpets beneath high-density turbidity currents ( $T_{B-2}$ ; Kuenen 1966; Leclair and Arnott 2005; Sumner et al. 2008). Fine-scale planar laminations produced by dilute flows ( $T_{B-3}$ ) and high-density flows ( $T_{B-2}$ ) may be very difficult to distinguish in the field or laboratory deposits (Fig. 4; Talling et al. 2012). Stepped planar laminations ( $T_{B-1}$ ) characteristically occur below massive ( $T_A$ ) sandstone intervals, and are most likely deposited incrementally by high-density turbidity currents (Hiscott and Middleton 1979, 1980; Lowe 1982), although in the Marnoso-Arenacea Formation they lack inverse grading (Sumner et al. 2012).

### Cross-Laminated ( $T_C$ ) Sandstone

Ripple-scale and dune-scale cross-laminated ( $T_C$ ) sandstones provide unambiguous evidence for deposition by low-density turbidity current (Simons et al. 1965; Harms and Fahnestock 1965; Allen 1982; Baas 1994; Southard 1991; Talling et al. 2012). Overlying planar-laminated siltstones ( $T_D$ ) are most likely also deposited by dilute near-bed flow (Amy and Talling 2006; Talling et al. 2012).  $T_D$  divisions are rarely seen in these Marnoso-Arenacea Formation beds.

### Turbidite Mudstone ( $T_E$ )

Turbidite mudstone ( $T_E$ ) can be clearly differentiated from hemipelagic mudstone in the Marnoso-Arenacea Formation based on the texture, color, and fossil content of the deposits (Talling et al. 2012a). Turbidite mudstone can be divided into laminated and graded ( $T_{E-1}$ ), massive and graded ( $T_{E-2}$ ), and massive and ungraded ( $T_{E-3}$ ) intervals (Piper 1978; Talling et al. 2012). Laminated mudstone ( $T_{E-1}$ ) is differentiated from very fine sandstone and coarse siltstone laminated intervals of the Bouma's  $T_D$  division on the basis of the modal grain size.  $T_E$  intervals have been deposited from a mud density flow which can be initially fully turbulent and dilute, but may also form a denser fluid mud layer that consolidates *en masse* (Talling et al. 2012).

### Grouping of Lithofacies and Down-Flow Facies Tracts

Lithofacies (Table 1) were grouped initially into the following four classes: (i) turbidite mudstone ( $T_E$ ), (ii) turbidite sandstone ( $T_A$  and  $B$ ), (iii) turbidite sandstone clearly deposited by dilute flow ( $T_C$  and  $D$ ), (iii) cohesive (mud-rich) debrite sandstone ( $D_M$ ), and (iv) clean sandstone debrite ( $D_{CS}$ ). Bed thickness is distinctly bimodal in the Marnoso-Arenacea Formation (Talling 2001), and thinner beds ( $< 40$  cm) tend to comprise only  $T_{CD}$ , together with turbidite mudstone ( $T_E$ ). Thicker beds ( $> 40$  cm) typically comprise  $T_{AB}$ , and sometimes  $D_M$  or  $D_{CS}$ , together with overlying  $T_{CD}$  intervals and turbidite mudstone ( $T_E$ ). Previous work grouped bed geometries into a series of facies tracts (see Mutti 1992) that capture the presence and arrangement of different lithofacies in the bed along a down-flow transect (Fig. 5; Amy and Talling 2006; Talling et al. 2012, 2013a, 2013b).

### Numerical Modeling

We present a mathematical model to illustrate how the deposit shape is influenced by particle concentration and hindered settling. This modeling is not intended (nor is it possible) to simulate all aspects of the flows that were responsible for the Marnoso-Arenacea beds, but rather to demonstrate some of the generic controls on flows that may have emplaced these deposits. The important general point is how the shape of the deposit is influenced by hindered settling as near-bed sediment concentrations increase. The model is applied to the depositional part of these flow events (i.e., that formed the beds that extend continuously across our study area). The starting point for modeling is taken at the beginning of our basin-plain outcrops, and it does not simulate earlier (possibly erosive) phases of flow.

We employ a depth-averaged formulation to study the steady, two-dimensional, spatial development of a turbidity current associated with a sustained source delivering a volume flux of fluid per unit width,  $q$ , with depth-averaged concentration of sediment,  $\phi_0$ . Models of this type have been used extensively for these flows (see, for example, Parker et al. 1986 and Falcini et al. 2009), although often the flow is assumed to be sufficiently dilute so that hindered settling plays only a negligible role. The basic assumption is that the flow is relatively shallow, so that its streamwise extent far exceeds its depth. This implies that the vertical accelerations are negligible and the pressure adopts a locally hydrostatic distribution. Thereafter the governing equations for fluid and sediment mass conservation and for momentum balance are depth-averaged to yield equations that govern the development of the layer-averaged quantities. A critical discussion of all of the modeling assumptions is given below.

The suspension comprises sedimentary particles with settling velocity  $v_{s\phi}$ , which is related to their excess density and size. This settling velocity is the terminal velocity through an otherwise quiescent, dilute suspension. As will be argued below, “hindered settling” effects reduce this settling velocity due to the nearby presence of other suspended particles. The density of the interstitial fluid is denoted by  $\rho$ , the excess density of the solids by  $\Delta\rho$ , and the volume fraction of solids by  $\phi$ , so that the density of the current is given by  $\rho_c = \rho + \Delta\rho\phi$ . Because part of our results concern hindered settling in which the concentrations of particles are relatively high, we do not assume that the presence of the suspended particles contribute negligibly to the overall density. This regime would correspond to the often studied Boussinesq case for which  $\Delta\rho\phi/\rho \ll 1$ . Instead, as will be shown below, we explicitly account for conservation of mass in each phase and derive an expression for momentum balance in which the bulk density of the current may vary. We further denote the steady, depth-averaged flow velocity, thickness of the flowing layer, and volume fraction of suspended particles by  $u(x)$ ,  $h(x)$ , and  $\phi(x)$ , where  $x$  is the downstream distance, while the deposit grows at rate  $dh/dt$ . In this analysis do not treat the temporal development of these flows, focusing

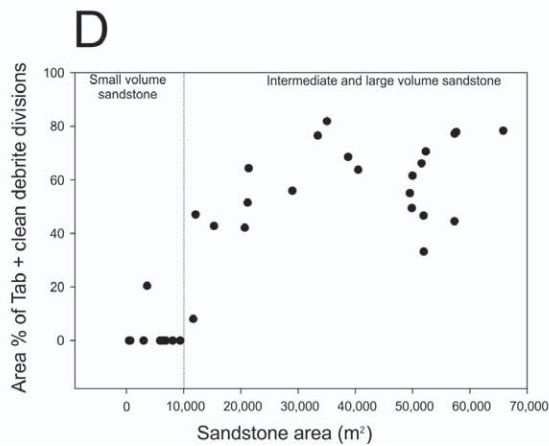
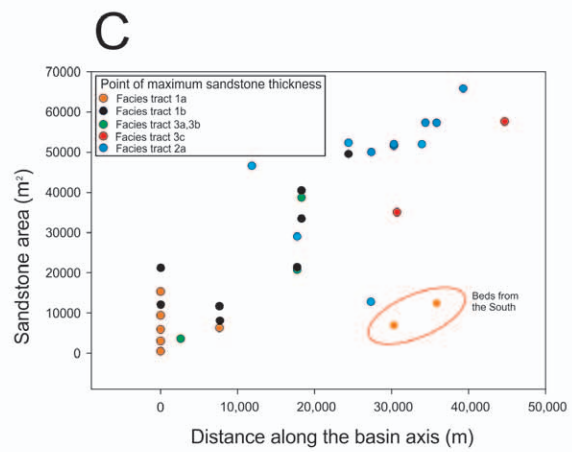
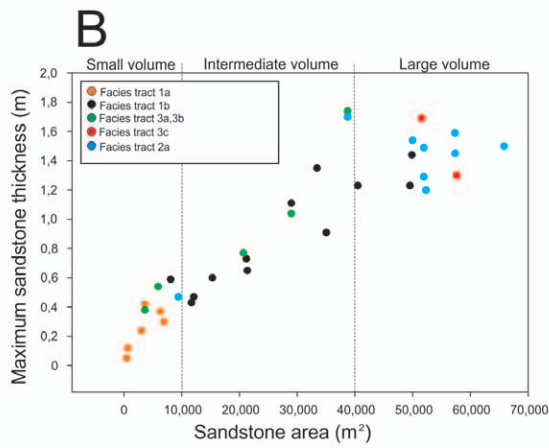
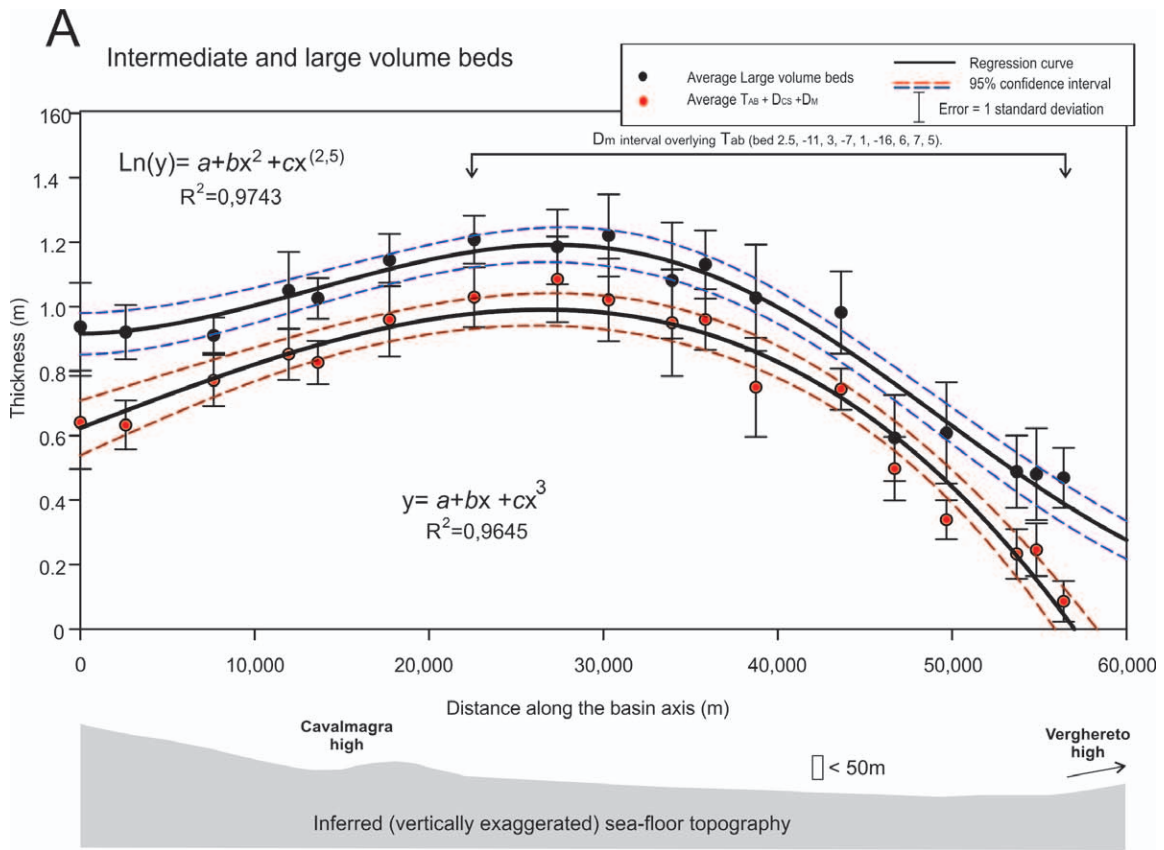


TABLE 2.—Regression curves for beds with different volume and facies tract. The regression parameters and the regression coefficient ( $R^2$ ) are indicated.

Figure	Volume	Facies Tract	Regression Curve	Parameters			$R^2$
				$a$	$b$	$c$	
8a	Small	1a,3a	$y = ae^{-bx}$	0.2413	3.25E-05		0.8947
11a	Small	1a	$y = ae^{-bx}$	0.2631	3.92E-05		0.9589
11b	Small	3a	$y = ae^{-bx}$	0.4935	0.0001		0.9476
10a	Intermediate and large	1b,2a,3a,3b,3c	$\text{Ln}(y) = a + bx^2 + cx^{(2.5)}$	-0.0876	1.77E-09	-8.60E-12	0.9743
11c	Intermediate and large	1a,1b	$\text{Ln}(y) = a + bx^2 + cx^{(2.5)}$	-0.2268	1.34E-09	-7.55E-12	0.9096
11d	Intermediate and large	2a	$\text{Ln}(y) = a + bx^2 + cx^{(2.5)}$	-0.2462	1.86E-09	-8.56E-12	0.8999
11e	Intermediate and large	3a,3b	$\text{Ln}(y) = a + bx^2 + cx^{(2.5)}$	-0.1557	5.23E-09	-3.73E-11	0.9681
11f	Large volume	3c	$\text{Ln}(y) = a + bx^2 + cx^{(2.5)}$	-0.2032	2.22E-09	-9.91E-12	0.9046
10a	Tab intermediate and large	1b,2a,3a,3b,3c	$y = a + bx + cx^3$	0.7067	1.68E-09	-7.98E-12	0.9645

instead on their steady form after the initial transient associated with the passage of the flow front.

Mass conservation of both phases accounts for transport in the flowing current and accumulating deposit; the latter is assumed to consist of particles with a constant volume fraction  $\phi_m$  that corresponds to the maximum packing fraction. Additionally water may be entrained into the current at its upper interface with the surrounding fluid. Thus fluid conservation for both the current and the deposit is expressed as

$$(1 - \phi_m) \frac{d\eta}{dt} + \frac{\partial}{\partial x}(uh(1 - )) = Eu, \tag{1}$$

where the right-hand side of (1) represents the rate of entrainment of surrounding fluid. On the assumption that the total sediment load of the current is not supplemented by additional erosion of pre-existing sediment layers, conservation of particles within the current and the deposit is given by

$$\phi_m \frac{d\eta}{dt} + \frac{\partial}{\partial x}(uh\phi) = 0. \tag{2}$$

Finally, balance of momentum for the flowing layer features fluid inertia, the depth-integrated streamwise pressure gradient, downslope acceleration, and basal drag, here represented through a quadratic drag law,

$$\frac{\partial}{\partial x} \left( \rho_c u^2 h + g \cos \theta \frac{\phi h^2}{2} \right) = g \sin \theta h - C_D \rho_c u^2, \tag{3}$$

In this expression we have assumed that the normal stresses in the suspension are isotropic and that the streamwise gradients of the deposit are much smaller than the underlying gradient of the seafloor. Furthermore, and importantly for flows with relatively high volume fractions of particles, we allow the bulk density of the current,  $\rho_c$ , to vary. To close this model, we must specify conditions at the interface between the deposit and the current. Here we adopt a simple representation of the depositional processes and assume that the current is only depositional and that the volume fraction jumps from maximum packing in the bed to the basal concentration in the current, denoted by  $\phi_b$ . Conservation of mass across the moving depositional interface then demands (see, for example, Kynch 1952, Dorrell et al. 2011)

$$\frac{d\eta}{dt} = \frac{v_s \phi_b}{\phi_m - \phi_b}, \tag{4}$$

and this expression permits the rate of growth of the deposit to be evaluated.

We require parameterizations for rate of entrainment, the basal drag, the relationship between the basal and depth-averaged concentrations, and the hindered settling velocity. The entrainment coefficient, which represents the rate at which ambient water is mixed into the flowing layer, is denoted by  $E$  and treated as a function of the local Richardson number ( $Ri = g \cos \theta \Delta \rho \phi h / (\rho_c u^2)$ ). Parker et al. (1986) suggest that for dilute currents

$$E = \frac{E_0}{A + Ri}, \tag{5}$$

with constants given by  $E_0 \cong 0.0015$  and  $A \cong 0.02$  (see also Johnson and Hogg 2013), and we adopt this parameterization for non-Boussinesq currents. The basal drag is expressed as a quadratic drag law with drag coefficient  $C_D$ . Potentially  $C_D$  could depend on the flow variables, such as the Reynolds number, the volume fraction of particles, or some rheological parameters. Here for simplicity we assume that  $C_D$  is constant ( $C_D = 10^{-3}$ ), noting that other formulations could be included, as discussed below; they would affect the details of the dynamical balance, but not the essence of the model under investigation. Finally, we follow Parker et al. (1986) and relate the depth-averaged volume fraction is related to the basal volume fraction by  $\phi_b = r \phi$ , with  $r = 1.6$ . This linear relationship is a further idealization as potentially one might determine the ratio of the two volume fractions in terms of the Rouse number. Finally, the hindered settling velocity at the bed is given by

$$v_s = v_{s\infty} (1 - \phi_b)^n \tag{6}$$

Richardson and Zaki (1954) suggest that the exponent  $n$  is approximately equal to 5. At this stage having fully specified the governing equations 1–4, it should be noted that they reduce to those of Parker et al. (1986) when the concentration of particles in the current is sufficiently dilute.

We apply boundary conditions at the source ( $x = 0$ ) to this system of equations 2–4. These specify the volume flux per unit width,  $u(0)h(0) = q$ , the initial concentration  $\phi(0) = \phi_0$ , and the source Froude number,  $F_0$ , such that  $\rho_c u(0)^2 / (\Delta \rho g \cos \theta \phi(0)h(0)) = F_0$ .

←

FIG. 10.—Sandstone interval shape in intermediate-volume and large-volume beds (Fig. 6) along the Ridracoli thrust sheet (Fig. 1). **A**) Regression curve showing the average thickness of intermediate-volume and large-volume beds shown in Figure 6. The average thicknesses of different groups of lithofacies are shown for (i) Bouma divisions  $T_{AB}$  and clean sandy debrite ( $D_{CS}$ ), and (ii) Bouma divisions  $T_{CD}$ . The 95% confidence limit and the standard deviation of sandstone thickness in each section are shown. The regression coefficients are shown in Table 2. **B**) Maximum sandstone thickness plotted against the sandstone cross-sectional area on the Ridracoli thrust sheet. **C**) Position of the sandstone thickness along the basin axis, plotted against the sandstone cross-sectional area. **D**) Area percentage of high-density basal  $T_{AB}$  and/or clean-debrite divisions ( $D_{CS}$ ) in beds with increasing sandstone area.

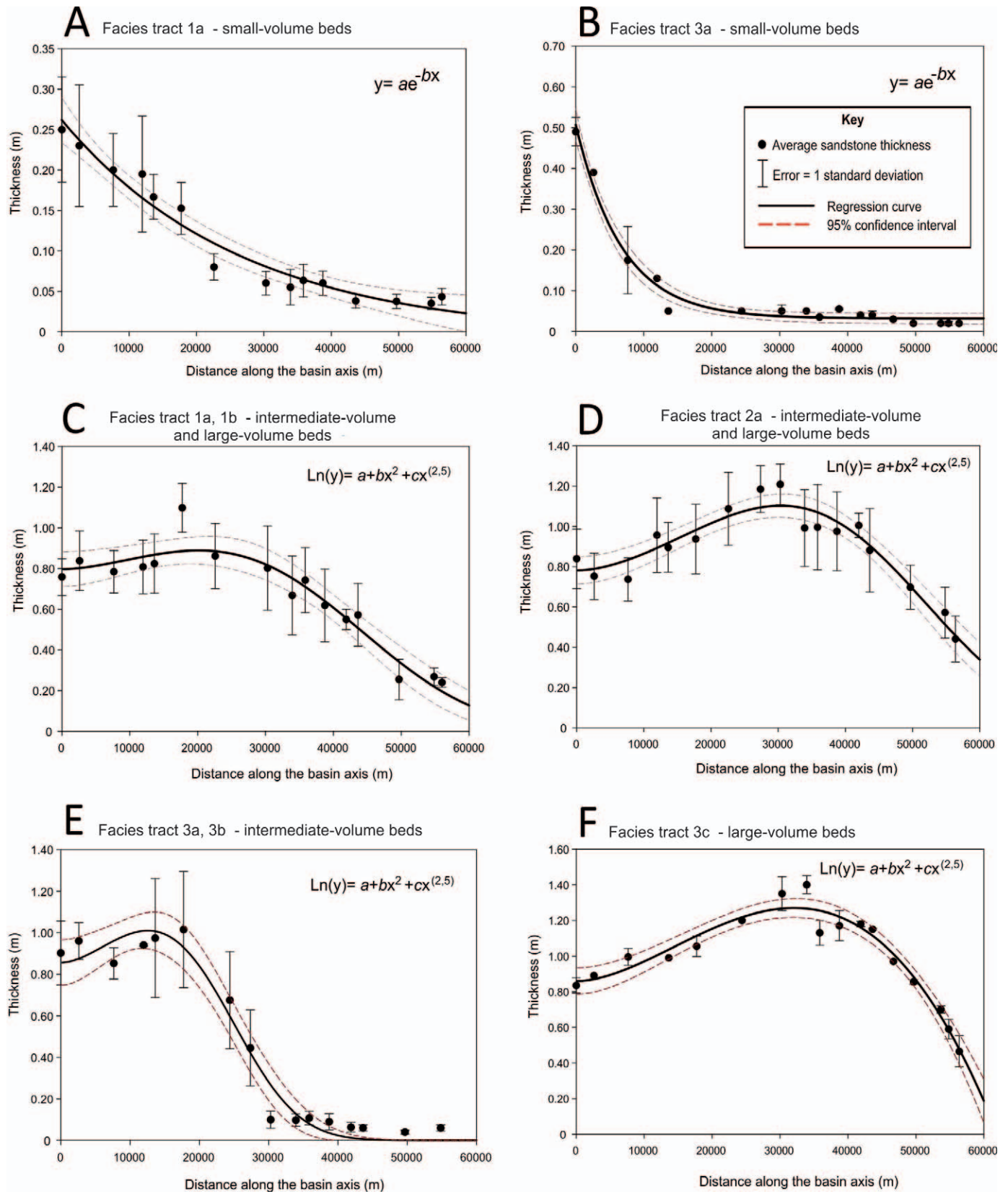


FIG. 11.—Regression curves showing the average thickness of beds with different facies tract shown in Figure 10. Also shown are 95% confidence limits for the regression line of average thickness with distance. The average thicknesses of different groups of lithofacies are shown for **A**) small-volume beds with facies tract 1; **B**) small-volume beds with facies tract 3a; **C**) intermediate-volume and large-volume beds with facies tract 1a and 1b; **D**) intermediate-volume and large-volume beds with facies tract 2a; **E**) large-volume beds with facies tracts 3a, b **F**) large-volume beds with facies tract 3c. The 95% confidence limit and the standard deviation of sandstone thickness in each section are shown. The regression coefficients are shown in Table 2.

It is advantageous to analyze these equations using the following dimensionless variables. The natural scale for the downstream distances over which sedimentation occurs is  $q/v_{s\infty}$ , while the initial density-induced velocity scale is  $u_b = (gq\cos\theta\Delta\rho\phi_0/\rho)^{1/3}$  and the scale of the volume fraction is  $\phi_0$ . Thus the following set of dimensionless variables are introduced

$$\{X, U, H, \psi, \psi_b\} = \left\{ \frac{v_{s\infty}}{q} x, \frac{u}{u_b}, \frac{u_b}{q} h, \frac{\phi}{\phi_0}, \frac{\phi_b}{\phi_0} \right\}. \quad (7)$$

Eliminating the rate of deposit growth, we find that the dimensionless system is now given by

$$\frac{\partial}{\partial X}(UH(1-\psi)) = \frac{\Lambda}{A+Ri} U - (1-\phi_m) \frac{\phi_0\psi_b}{\phi_m-\phi_0\psi_b} (1-\phi_0\psi_b)^n, \quad (8)$$

$$\frac{\partial}{\partial X} \left( (1+\beta\psi)U^2H + \frac{1}{2}\psi H^2 \right) = \Omega(S\psi H - C_D(1+\beta\psi)U^2), \quad (9)$$

$$\frac{\partial}{\partial X}(UH\psi) = - \frac{\phi_m\psi_b}{\phi_m-\phi_0\psi_b} (1-\phi_0\psi_b)^n, \quad (10)$$

where  $Ri = \psi H((1+\beta\psi)U^2)$ . The dimensionless source conditions are given by  $U(0)H(0) = 1$ ,  $\psi(0) = 1$ , and  $(1+\beta)U(0)^2/H(0) = F_0$ . In these expressions, there are now three additional dimensionless parameters,  $\beta$ ,  $\Lambda$ , and  $\Omega$ , given by

$$\beta = \frac{\Delta\rho\phi_0}{\rho}, \quad \Lambda = \frac{E_0u_b}{v_{s\infty}}, \quad \Omega = \frac{u_b}{v_{s\infty}}. \quad (11)$$

Respectively, these measure the relative contribution of the initially suspended particles to the density of the fluid, the relative magnitude of fluid entrainment and the ratio of the buoyancy-induced velocity to the initial settling velocity. The flows under consideration are not necessarily initially dilute, and so this implies that the parameter  $\beta$  is of order unity ( $\beta \sim 1$ ). Typical sea-floor gradients are 0.05 degrees, and so we set  $S = 10^{-3}$ . Flows are hypothesized to have a typical initial volume flux per unit width  $q = 10^2 \text{ m}^2 \text{ s}^{-1}$ , with an initial concentration  $\phi_0 = 0.1$  (although the latter will be varied in the calculations that follow) and a settling velocity  $v_{s\infty} = 10^{-2} \text{ ms}^{-1}$ , (corresponding to sediment of approximate grain size 100  $\mu\text{m}$ ). This means that  $\Lambda \sim 1$  and  $\Omega \sim 10^3$ . Importantly, because  $\Lambda \sim 1$ , this implies that entrainment of fluid may be non-negligible along the path of the turbidity current.

Particles sediment out of the flow to form the deposit,  $\eta(x, t)$ . The dimensionless growth rate,  $D(X)$  is then given by

$$D = \frac{\phi_m}{v_{s\infty}\phi_0} \frac{d\eta}{dt} = - \frac{\psi_b(1-\phi_0\psi_b)^n}{(1-\phi_0\psi_b/\phi_m)} \quad (12)$$

The bed shape is then given by profiles for  $D(X)$ , and these are calculated below.

### Key Assumptions Underpinning the Numerical Model

This layer-averaged model entails a number of assumptions that need to be stated clearly. The model does not include sediment re-entrainment or erosion from the bed. This means that the modeled flows are always depositional for all grain sizes. The model cannot therefore reproduce the initial stages of powerful flows that erode or bypass sediment, as is sometimes observed in the field (Talling et al. 2007a; MacDonald et al. 2011; Stevenson et al. 2013). This could be amended to include an erosive flux of particles in equation 4, but this would add to the complexity of the analysis and is not pursued here.

The model represents drag through a constant drag coefficient, which is an appropriate representation for dilute flows at high Reynolds number;

the explicit effects of molecular viscosity are therefore neglected. For higher concentrations, the flow resistance might be provided by particle interactions, and this would necessitate an alternative parameterization of the drag. This formulation also neglects the effects of yield strength that may cause non-Newtonian flows to come to an abrupt halt at their margins. Furthermore the transition between a fluid phase and a solid phase has been straightforwardly handled via a mobile depositional interface; flows with cohesive properties might arrest in different ways. Together these mean that the model is poorly suited to simulating the behavior of flows in which cohesive forces play a strong role, and it is not applied to turbidite mud or debris-flow deposits.

The seafloor is assumed to have a constant gradient of approximately  $0.05^\circ$  ( $S = 10^{-3}$ ), which is typical for modern basin plains (Talling et al. 2007, 2012). Quantitative changes in gradient across the Marnoso-Arenacea basin floor are poorly constrained (see later discussion), and variations in sea-floor gradient are not included here. Model results are based on flows with one grain size (100  $\mu\text{m}$ ), although the Marnoso-Arenacea flows contained a wide range of grain sizes, and in some situations it is known that polydispersity can strongly affect the properties of sediment suspensions (see, for example, Harris et al. 2002, Dorrell et al. 2011). The model is for a steady state; it is likely that oceanic flows will show some unsteadiness, especially during their initiation and cessation. However, the investigation of steady flows helps to draw out the other controls on deposit.

## RESULTS

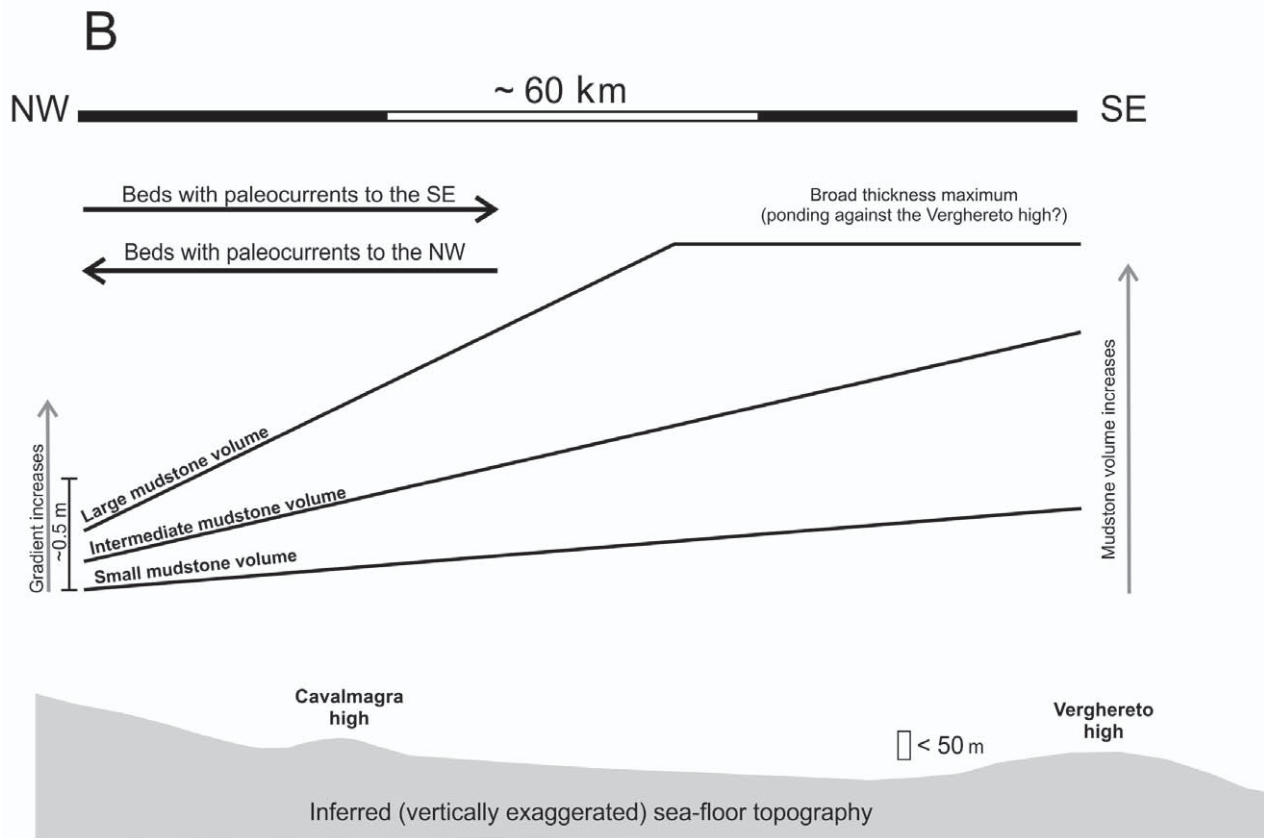
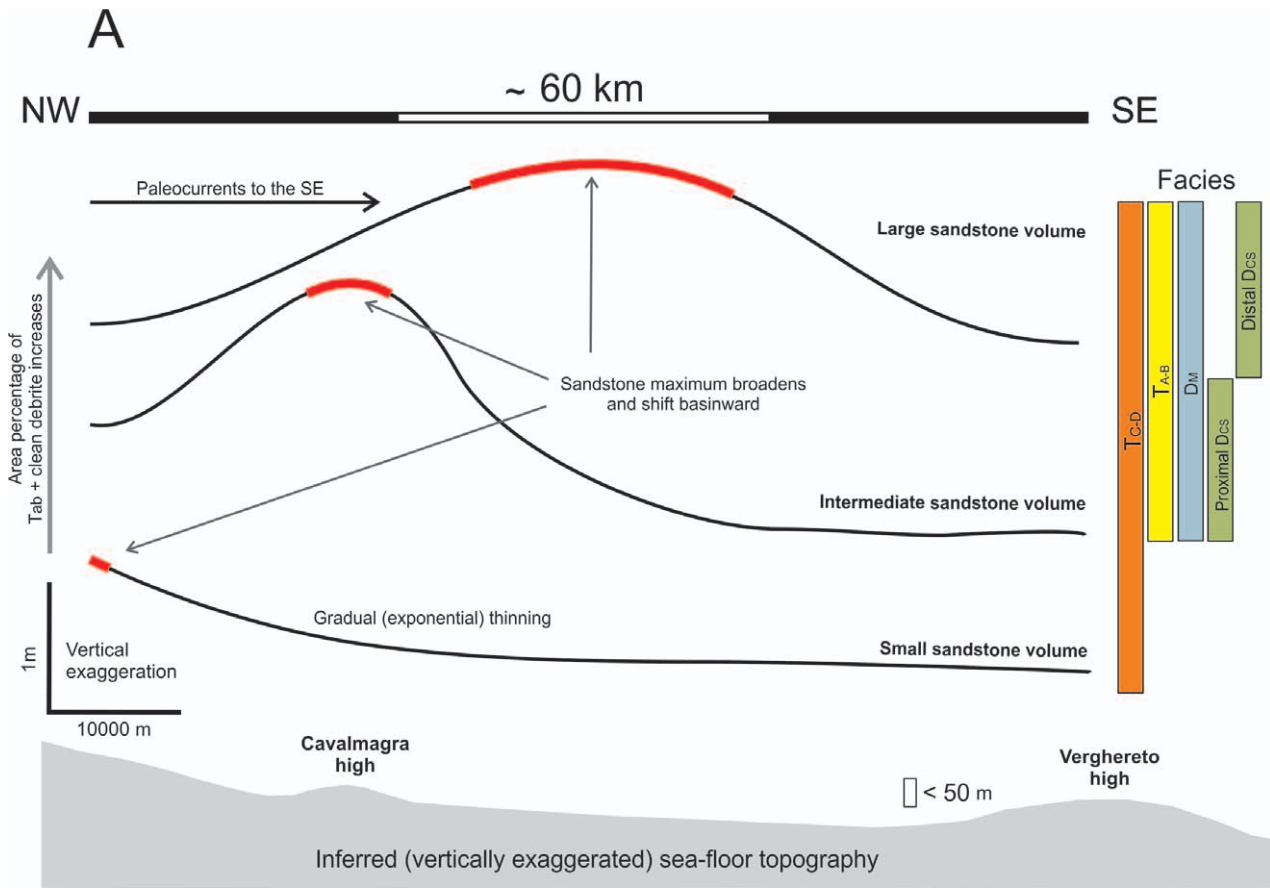
Bed geometries are organized initially by volume (Fig. 6), and then according to down-flow facies tract (Fig. 7). These two figures illustrate both changes in deposit geometry with increasing flow volume, and modes of flow behavior that may not coincide with increasing bed volume. Scaling of the thickness axis on these plots varies to aid comparison of shape, such that maximum bed thickness corresponds to a similar length along this axis (Figs. 6, 7). The extreme vertical exaggeration of deposit shape (typically 30,000 times) should be noted, as the real shape is much flatter and more tabular. The base of each bed is shown as a horizontal datum.

### Small-Volume Beds

Small-volume beds have a cross-sectional sandstone area of  $< 10,000 \text{ m}^2$ . Seven of these small-volume beds originated from the northwest, and they show a consistent shape (Figs. 6, 7). Their sandstone thickness declines rapidly over  $\sim 20\text{--}30 \text{ km}$  in an approximately exponential fashion, and sandstone thickness is then relatively constant across the distal part of the Ridracoli Element (Fig. 8A). Sandstone in these beds tends to be fine grained ( $< 187 \mu\text{m}$ ), and there is little visible fining in a down-basin direction (Fig. 9A). Two small-volume beds originated from the southeast and flowed across the basin plain in the opposite direction (beds 7.1 and 1.2.3), most likely uphill. Their sandstone interval has a relatively tabular shape across the entire Ridracoli thrust sheet. In general, the average shape of small-volume beds thins in a near exponential fashion (Fig. 8A), with their volume related to their thickness at the most proximal section (Fig. 8B). The rate at which their thickness declines appear to be related to their volume (Fig. 8C).

### Intermediate-Volume and Large-Volume Beds

Intermediate-volume beds have a sandstone cross-sectional area of 10,000 to 40,000  $\text{m}^2$ , whilst large-volume beds have a sandstone cross-sectional area  $> 40,000 \text{ m}^2$ . All of these beds originated from the northeast, with the exception of Colombine-1 bed, which was sourced from the southeast. The sandstone interval of the Colombine-1 bed has a tabular shape, similar to that of small volume beds (beds 7.1 and 1.2.3)



with a similar southeastern provenance. It is the only intermediate-volume bed whose sandstone comprises only  $T_{CD}$  intervals. All of the other intermediate-volume and large-volume beds contain intervals of massive ( $T_A$ ) or planar laminated ( $T_B$ ) turbidite sandstone, or debrite sandstone that can be mud-rich ( $D_M$ ) or clean ( $D_{CS}$ ). This contrasts with the dominance of  $T_{CD}$  sandstone intervals in small-volume beds (Fig. 6).

Sandstone shape in intermediate-volume and large-volume beds differ significantly from that in small volume beds. A broad thickness maximum characterizes larger-volume sandstones (Fig. 10), and this thickness maximum moves basinward as sandstone volume increases. Intermediate-volume and large-volume beds contain massive ( $T_A$ ) and planar-laminated ( $T_B$ ) sandstone intervals that are lacking in the small-volume beds. It is the massive and planar-laminated sandstone intervals ( $T_{AB}$ ) that mainly determine the overall sandstone shape, in that they are often much thicker than overlying  $T_{CD}$  intervals. The shape of the basal  $T_{AB}$  (plus clean debrite) division can be approximated by a third-order polynomial function  $y = a + bx + cx^3$  (Fig. 10A, Table 2). The overall shape of intermediate and large beds is described by the function  $\ln(y) = a + bx^2 + cx^{(2.5)}$  (Fig. 11A, 12, Table 2). Unlike exponential functions for small-volume beds, these formulations cannot be interpreted in terms of physical flow processes. However, they proved the necessary flexibility to capture the shape of sandstone beds for varying volume and facies tract.

The maximum thickness and volume of the sandstone intervals are broadly related (Fig. 10B), and the thickness maximum tends to migrate farther down the basin as the volume increases (Fig. 10C). There is little correlation between sandstone volume in intermediate and large volume beds and their initial thickness at the most proximal section (Fig. 6). Intermediate-volume and large-volume beds have significantly larger maximum grain sizes than small-volume beds (Fig. 9). Rates of down-basin fining of maximum grain size can be rather slow, especially for large volume beds (Fig. 9). However, more rapid fining is observed near the down-flow termination of  $T_{AB}$  or clean debrite sandstone ( $D_{CS}$ ) interval (Fig. 9).

#### *Sandstone Shape Subdivided According to Facies Tract*

The geometry of intermediate-volume and large-volume sandstone beds display a series of facies tracts, which capture different modes of flow behavior and evolution (Fig. 5; Amy and Talling 2006; Talling et al. 2007a, 2007b; Talling et al. 2012, 2013a, 2013b). Facies tract 1, 2a, 3a, 3b, and 3c can be described by the same characteristic function  $\ln(y) = a + bx^2 + cx^{(2.5)}$  (Fig. 11). However, the rate of proximal thickening and position of the thickness maximum differs for each facies tract (Fig. 12).

Small-volume beds typically comprise only  $T_{CD}$  intervals overlain by turbidite mudstone, comprising facies tract 1a ( $T_E$ ; Fig. 6). The only exceptions are beds -9 and -12, in which a proximal clean sandstone debrite ( $D_{CS}$ ) pinches out abruptly, and they are assigned to facies tract 3a (Fig. 5). Intermediate-volume and large-volume beds lacking debrites (facies tract 1b) maintain an approximately constant thickness for 20 km, followed by gradual thinning that is driven by changes in the  $T_{AB}$  interval thickness (Fig. 10). Only low-strength clast-poor cohesive debrites (facies tract 2a) are seen in this study area, with higher-strength cohesive debris flows found elsewhere in the basin plain (Talling et al. 2013b). The addition of the cohesive debrite above underlying turbidite sandstone produces a more pronounced thickness maximum in mid basin

(Fig. 11D). More rapid thinning of sandstone intervals can occur due to the pinch-out of clean debrite intervals ( $D_{CS}$ ) in facies tract 3a and 3b.

#### *Turbidite Mudstone Intervals*

The shape of turbidite mudstone ( $T_E$ ) intervals for progressively larger-mudstone-volume beds is presented in Figure 13. In many cases mudstone constitute most of the bed. Mudstone intervals have a consistent shape, with an increase in thickness from northeast to southwest for beds derived from both the northeast and the southwest (Fig. 14). Local thickness variations are not due to erosion by successive flows, because each mudstone interval measured in this study is capped by an interval of hemipelagic marl. The two largest-volume mudstone beds (bed 6 and Colombine) have a broad thickness maximum in the central and distal part of the Ridracoli element.

#### *Numerical Modeling*

Modeling results are presented that explore how turbidite sandstone shape (expressed as a dimensionless rate of deposit growth) varies as sediment concentration increases from volume fractions of 0.05 to 0.3. Hindered settling occurs at higher sediment concentrations, reducing particle settling velocity and affecting the flux of settling particles. Model results are based on a constant sea-floor gradient of  $0.05^\circ$ , a steady input flux, and a single grain size.

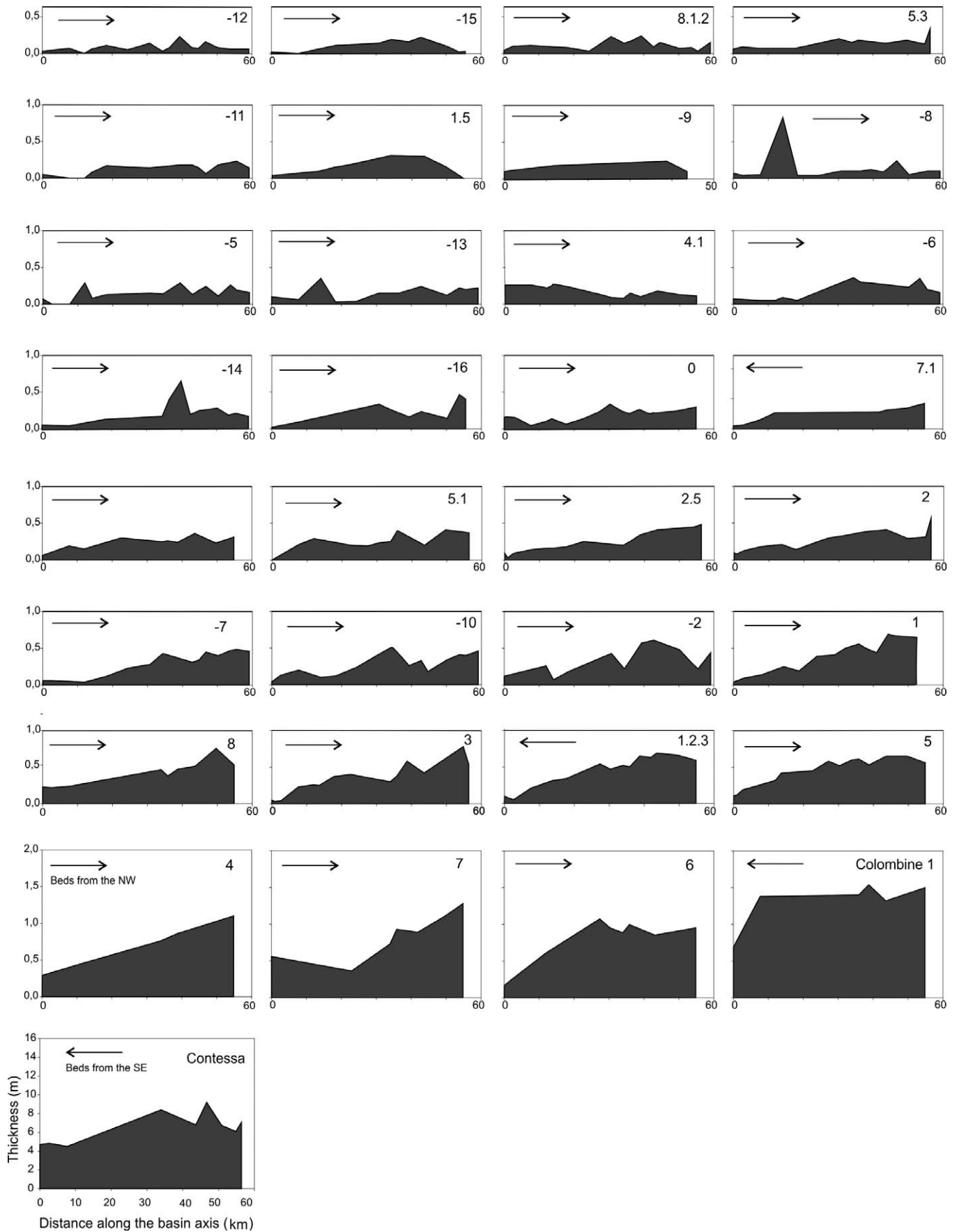
#### DISCUSSION

##### *To What Extent Did Seafloor Topography Control Deposit Shape, and Can We Tell?*

It is reasonable to ask whether changes in seafloor gradient were a dominant control on the bed geometries analyzed here. This is because studies of recent deposits below the modern seafloor show that changes in gradient can strongly influence bed shape, or indeed whether a flow is depositional or erosional (e.g., Talling et al. 2007a; Wynn et al. 2010; Stevenson et al. 2013). Field observations from ancient outcrops can only place qualitative constraints on seafloor gradients. The continuous ("layer-cake") stratigraphy suggests that gradients did not change substantially, and were most likely less than approximately  $0.05^\circ$  by comparison to studies of modern basin plains. Changes in seafloor gradient are likely to affect a number of adjacent beds in a consistent fashion, providing a way of identifying their effects. Consistent but small fractional changes in bed thickness suggest that a subtle interbasinal high near the Cavalmagra section (Fig. 2) was present within the Ridracoli Element. The consistent location at which clean-sand debrites terminate (Talling et al. 2013a), or the consistent location of cohesive debrites (Talling et al. 2013b), is most likely partly due to changes in gradient. Consistent thickening of the entire correlated sequence within the central part of the Ridracoli element (Fig. 2; Amy and Talling 2006; Talling et al. 2013a, 2013b) may indicate a subtle topographic low, or area of lower gradient. Comparison of deposit geometries for flows with opposing directions provides a second test for the effects of changing seafloor gradient, as one direction must be up hill. This suggests that the shape of mudstone intervals is much more strongly affected by basin topography than the shape of sandstones, as a consistent mudstone shape is found for flows initially travelling in both directions. Sandstone deposition is more weakly affected by basin topography, although flows from the southeast tend to produce more tabular deposits.

←

FIG. 12.—A) Scheme summarizing the variations of bed shape and internal facies architecture for progressively larger-volume sandstone beds. B) Scheme summarizing the variations of bed shape for progressively larger-volume mudstone beds, and their relationship with the sea-floor topography.



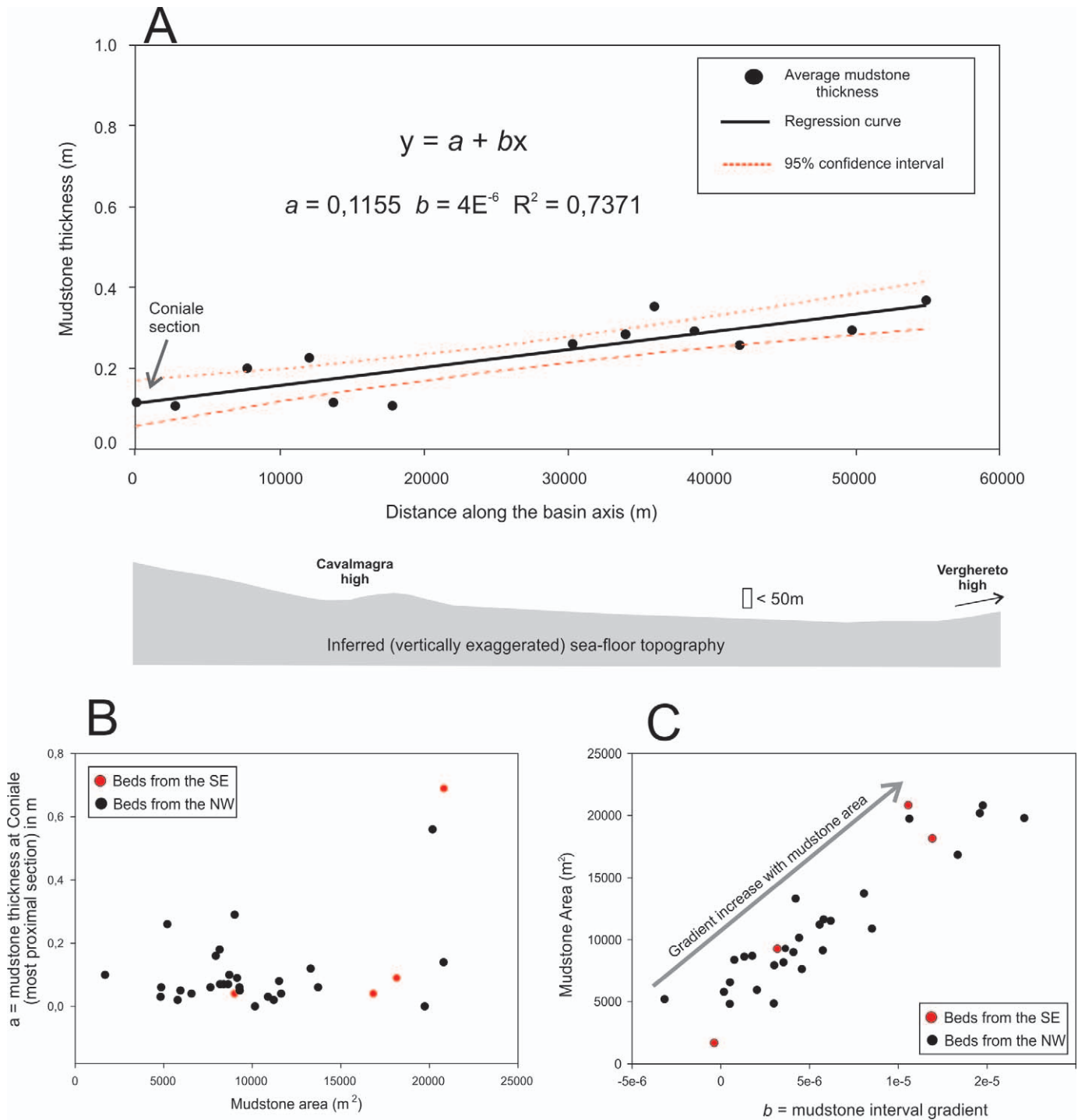


FIG. 14.—A) Regression line describing the lateral thickness variations in mudstone-interval thickness. The prediction interval calculated at a 95% confidence limit is also plotted. B, C) Comparison of  $a$  and  $b$  parameters of the regression line to the calculated mudstone cross-sectional area for each bed.

←

FIG. 13.—Diagrams illustrating the lateral changes in mudstone (TE) thickness in the 32 turbidite beds from the above-Contessa and below-Contessa intervals, along the Ridracoli Element in a direction subparallel to paleoflow (Fig. 1). Diagrams are ordered according to increasing mudstone cross-sectional area (a proxy for mud volume). Note that the vertical exaggeration is very large, typically about 1:30,000.

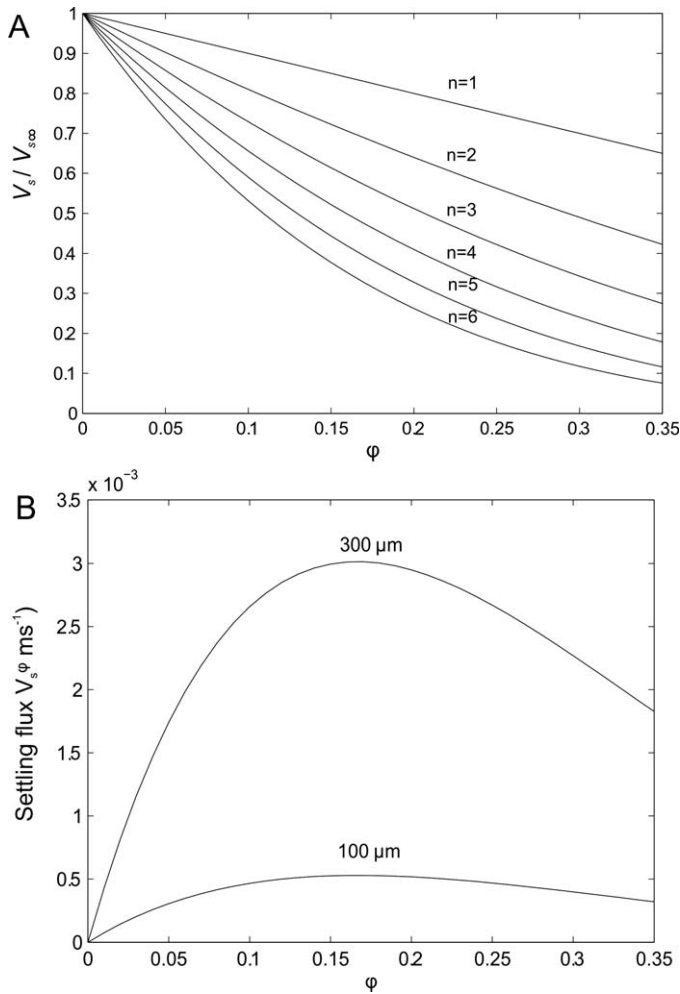


FIG. 15.—**A**) The settling velocity relative its dilute value,  $v_s/v_{s,oc}$  as a function of volume fraction,  $\phi$ , using the hindered settling formulation of Richardson and Zaki (1954)  $v_s = v_{s,oc}(1-\phi)^n$ . For various values of  $n$ . **B**) The settling flux of sediment  $v_s\phi$  as a function of volume fraction for sand of two grain sizes. Here  $n = 5$  in the formulation of Richardson and Zaki (1954). The peak settling flux occurs at intermediate sediment volume concentrations.

#### Shape of Small-Volume Sandstones—Dilute and Dissipative Flow

Small-volume sandstones in thin beds in the Marnoso-Arenacea sequence are dominated by cross-laminated ( $T_C$ ) intervals that provide evidence of deposition from dilute flow (Talling et al. 2012). The almost exponentially thinning shape of these small-volume sandstones is also similar to the general shape of dilute flow deposits in the layer-averaged model.

Similar facies comprise the thin beds that dominate levees formed adjacent to submarine channels. Submarine levee packages also tend to thin away from levee crests in a near exponential fashion, although this shape can sometimes be described by a power-law relationship (Skene et al. 2002; Skene and Piper 2005; Kane et al. 2007, 2010; Dykstra et al. 2012; Birman et al. 2009; Nakajima and Kneller 2011). A near exponential decay in deposit thickness characterizes the deposits of dilute flows in flume experiments and numerical models that decelerate with distance (i.e., they are dissipative; Talling et al. 2007b). It was therefore proposed by Talling et al. (2007b) that a near exponential decay of deposit thickness is a characteristic feature of dilute flows that decelerate along their flow path (dissipate). However, the  $e$ -folding distance (that in

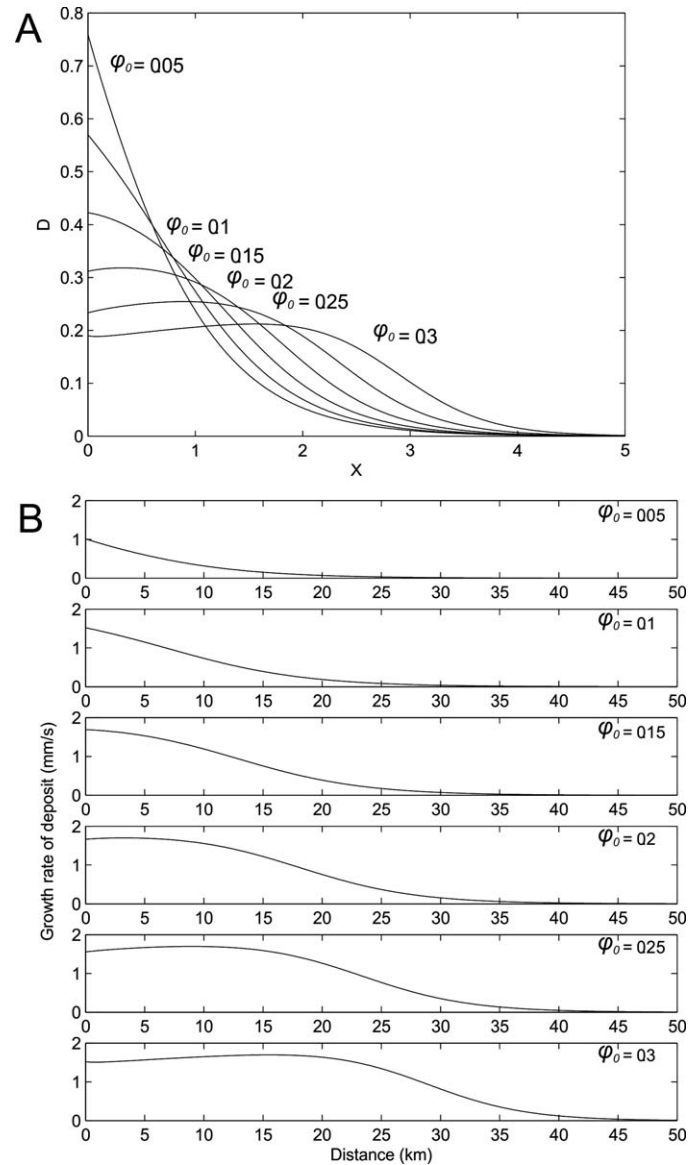


FIG. 16.—**A**) The dimensionless growth rate of the deposit,  $D$ , as a function of dimensionless distance,  $X$  for varying concentration at source ( $\phi_0$ ). For these plots we have used the following parameter values:  $q = 10^2 \text{ m}^2 \text{ s}^{-1}$ ,  $v_{s,oc} = 10^{-2} \text{ ms}^{-1}$ ,  $S = 10^{-3}$ ,  $C_D = 10^{-3}$ ,  $\Delta\rho/\rho = 1.65$ ,  $r = 1.6$ ,  $\phi_m = 0.6$ ,  $F_0 = 0.59$ . **B**) The dimensional growth rate  $dh/dt$  as a function of distance  $x$  for varying concentration at source ( $\phi_0$ ). For these plots we have used the following parameter values:  $q = 10^2 \text{ m}^2 \text{ s}^{-1}$ ,  $v_{s,oc} = 10^{-2} \text{ ms}^{-1}$ ,  $S = 10^{-3}$ ,  $C_D = 10^{-3}$ ,  $\Delta\rho/\rho = 1.65$ ,  $r = 1.6$ ,  $\phi_m = 0.6$ ,  $F_0 = 0.59$ .

which the bed thickness declines by 37%) seen in levee sequences and numerical or flume experiments is typically much shorter than that in the thin beds of the Marnoso-Arenacea Formation (Talling et al. 2007b). This more rapid decay of deposit thickness (shorter  $e$ -fold distance) most likely results from radial flow expansion or thinner flow (Talling et al. 2007b).

#### How Does Flow Concentration and Hindered Settling Affect Sandstone Shape?

We now explore how hindered settling from dense near-bed layers might influence deposit shape, and whether it can explain observed sandstone shapes. Hindered settling starts to occur at sediment volume

concentrations of  $\sim 10\%$  as grain interactions become important (Bagnold 1954), and its effects become increasingly (nonlinearly) important as volume concentrations increase further (Fig. 15; Richardson and Zaki 1954). Talling et al. (2007a) proposed that hindered settling was the primary reason for the broad thickness maximum observed in larger-volume beds dominated by massive ( $T_A$ ) and planar-laminated ( $T_B$ ) sandstone intervals. This hypothesis was based in part on observation that planar-laminated ( $T_B$ ) intervals were typically laterally equivalent to massive ( $T_A$ ) intervals of similar thickness, and there is consensus that  $T_A$  intervals are more clearly deposited by dense flows.

This hypothesis was tested using the layer-averaged flow model. A series of model runs were undertaken with a constant sea-floor gradient of  $0.05^\circ$ , with a steady input flux, and using a single grain size. Model results are expressed initially as the dimensionless rate of deposit growth,  $D(X)$ , (see Eq. 12) for a wide range of source volume fractions,  $\phi_0$  (Fig. 16). The distinctive shape of  $T_A$  and  $T_B$  sandstone intervals characterized by a broad thickness maximum is well reproduced in numerical models that include hindered settling (Fig. 16). Dilute sediment flows have deposits whose thickness decays almost exponentially (Fig. 16). The broad thickness maximum only appears once elevated sediment concentrations result in hindered settling (Figs. 15, 16).

The sediment accumulation rate is proportional to the product of near-bed sediment concentration and the sediment settling velocity. The broad thickness maximum results from initially strongly hindered settling, which results in low sediment accumulation rates. Intermediate sediment concentrations and settling rates produce the highest sediment accumulation rates, which form the broad thickness maximum. Reduced sediment concentrations farther from source cause a transition into non-hindered settling from dilute flow, which produced a distal deposit that thins in a near exponential fashion. We can show that the deposit thickens with downstream distance when the instantaneous bed concentration is sufficiently large ( $\phi_b > 1/(n+1)$ ), where  $n$  is the exponent in the Richardson-Zaki settling velocity equation (Figs. 15, 16).

#### *What Determines the Distance to the Deposit Maximum?*

The distance to the deposit maximum increases for flows with a higher input flux ( $q$ ), which are initially thicker or faster. An increase in grain size and hence settling rate ( $v_{sc}$ ) tends to reduce the distance to the thickness maximum. Higher rates of fluid entrainment also increase the distance to the deposit thickness maximum.

The distance to the thickness maximum is 10 to 40 km in the field dataset, although this depends on the location of the most proximal outcrop (i.e., where  $x = 0$ ). The deposit maximum occurs at dimensionless distances of 1 to 4 in the model runs (Fig. 16A). This implies that the ratio of  $q/v_{sc}$  is  $\sim 10^4$  m, if the model is to reproduce the distance to the deposit maximum seen in the field. Using a terminal sediment settling velocity ( $v_{sc}$ ) of  $\sim 10^{-2}$   $\text{ms}^{-1}$  for a  $100 \mu\text{m}$  grain (Fig. 16B), this implies an input flux per unit width ( $q$ ) of  $\sim 100 \text{ m}^2 \text{ s}^{-1}$ , which would equate to flow that is 65 m thick and travelling at  $\sim 1.6 \text{ ms}^{-1}$ . The distance to the deposit thickness maximum seen in the field can therefore be reproduced by reasonable values of the parameters  $q$  and  $v_{sc}$  (Fig. 16B). See Talling et al. 2014 for a summary of turbidity current thicknesses and speeds measured in the field. Sediment deposition was found to occur below speeds of  $\sim 1.6$  m in the experiments of Sumner et al. (2009), so flows travelling at such speed might be expected to be depositional. For these parameter values the entrainment parameter is approximately 0.1.

#### *Deposition Rates, Flow Duration, and Lithofacies*

Rates of sediment accumulation can be estimated at the deposit thickness maximum. Assuming a value of  $\sim 10^{-2}$  m/s for  $v_{sc}$  (for a  $100 \mu\text{m}$  grain),  $r = 1.6$  (Parker et al. 1986), and a porosity of  $\sim 0.5$  in the deposit, this implies that peak nondimensionalized sediment accumula-

tion rates ( $D$ ) of  $\sim 0.2$  to  $0.45$  seen in the model runs (Fig. 16) equate to sediment accumulation rates of  $\sim 0.2 \text{ mm s}^{-1}$ . Flows that lasted  $\sim 50$  minutes would be needed to build up sandstone intervals that had peak thicknesses of  $\sim 1$  m, as seen in the field examples. Assuming a speed of  $\sim 1.6$  m/s, this 50 minute duration would imply that the depositional part of the flow was  $\sim 3$  km in length, from its head to tail.

Laboratory experiments suggest that a sediment accumulation rate of  $\sim 0.44 \text{ mm s}^{-1}$  characterizes the boundary between the formation of massive ( $T_A$ ) and planar-laminated ( $T_B$ ) sand (Sumner et al. 2008). The sediment accumulation rates near the deposit thickness maximum seen in the model runs are therefore broadly consistent with deposition of massive or planar-laminated sandstone intervals, as is observed in the field (Fig. 16b).

#### *Comparison with Previous Work*

Most previous numerical studies of bed shape have assumed that flow is sufficiently dilute so that sediment settling is unhindered, and they have tended (Talling et al. 2007a) to produce deposit shapes whose thickness decreases monotonically down-flow in a quasi-exponential fashion (Zeng and Lowe 1997; Salaheldin et al. 2000; Felix 2001, 2002; Harris et al. 2002; Das et al. 2004; Gray et al. 2005; Falcini et al. 2009). A broadly similar continuously thinning shape characterizes most experimental turbidity current deposits (Talling et al. 2007a), including laboratory studies with both steady and nonsteady (lock release) inputs, and unimodal or polydisperse grain sizes (Bonnecaze et al. 1996; Gladstone et al. 1998; Woods et al. 1998; De Rooij and Dalziel 2001; Choux and Druitt 2002; Kubo 2004; Gray et al. 2005). It appears that dilute flows that decelerate spatially tend to produce deposit shapes that thin almost exponentially, as seen discussed previously when considering channel-levee deposits.

Tinterri et al. (2003) is one of the few previous modeling studies to include effects of hindered settling, and their model results suggest that a thickness maximum is a general feature of hindered settling. Their model differed from that presented here in key regards. It comprised a dense lower layer in which sand was liquefied, and from which hindered settling occurred (Tinterri et al. 2003). This type of liquefied dense flow most closely resembles clean-sand debris flow (that form  $D_{CS}$  or Tinterri et al.'s F5 facies; see Talling et al. 2012), rather than high-density turbidity currents (that form  $T_A$  or  $T_{B1\&2}$ ). This is consistent with the narrow thickness maximum in Tinterri et al.'s (2003) modeled deposits, which more closely resembles the shape of clean-sand debrites ( $D_{CS}$ ) than the broader thickness maximum of  $T_{AB}$  intervals within Marnoso-Arenacea beds.

#### *Alternative Hypotheses to Explain the Broad Thickness Maximum: Flow Carrying Capacity*

Modeling presented here shows that hindered settling provides a plausible mechanism to reduce sediment settling fluxes and produce thinner sand deposits in the proximal part of the bed and a broad thickness maximum (Fig. 16). However, there are other plausible mechanisms that may generate this type of deposit shape, which are not addressed. For instance, the model does not include resuspension of sediment from the bed, and changes in mass of sediment that the flow could suspend (its capacity; Kuenen and Sengupta 1970; Hiscott 1994). The initial stages of a flow may be sufficiently powerful to suspend all of the sediment that is carried by the flow, resulting in sediment bypass, potentially with erosion of the bed. As the flow speed and capacity then declines, there may be a region in which the sediment load in the flow is similar to the sediment carrying capacity of the flow. This would lead to an initial area of reduced sediment deposition and an increase in deposit thickness with distance, forming a thickness maximum. More generally, modeling presented here shows that hindered settling may produce a deposit shape with a broad thickness maximum, but there may be other processes that can also cause this type of shape.

## CONCLUSIONS

There are few studies that have documented the shape of individual submarine flow deposits. Here we show the shape of 32 individual submarine flow deposits in a down-flow direction in an ancient basin plain that lacks channels or even bed amalgamation. Field observations (including this “layer-cake” stratigraphy) suggest that seafloor topography was subdued in this basin plain, although quantitative constraints on changes in seafloor gradient cannot be measured. Despite the complexity of these deposits in this topographically simple basin-plain setting, there are distinct types of down-flow evolution (captured by facies tracts; Fig. 5). Sandstone intervals in thin beds with smaller volumes are typically dominated by cross lamination ( $T_C$ ). Their almost exponentially thinning shape is consistent with deposition from dilute and dissipative flows, which is consistent with the presence of migrating bedforms. This exponentially thinning shape resembles that seen in levee sequences adjacent to submarine channels, and deposits in dilute and dissipative laboratory and numerical models, although the rate of thinning of the Marnoso-Arenacea sandstones is rather slow. Thicker and larger-volume sandstone intervals in the Marnoso-Arenacea Formation are dominated by massive ( $T_A$ ) and planar-laminated ( $T_B$ ) sandstone, and they display a different shape with a broad thickness maximum. The results from a layer-averaged numerical model suggest that this shape records hindered settling from dense near-bed flow. This result is important because it suggests that both massive and planar-laminated sandstones were deposited from high-density turbidity currents. Many beds also contain sandstone intervals that can pinch out more rapidly, and were deposited by cohesive (muddy) or clean-sand debris flows. Their shape has been analyzed elsewhere (Amy et al. 2005; Talling et al. 2013a, 2013b). Deposition of turbidite mud is more strongly affected by basin-floor topography, in that a similar mudstone shape is generated by flows that traversed the basin plain in opposing directions. This unusual field data set suggests that planar-laminated ( $T_B$ ) sandstone intervals may record deposition from dense near-bed layers, which is important because they can also be formed by dilute flow in laboratory experiments.

## ACKNOWLEDGEMENTS

This work was part of a UK-TAPS project, funded by NERC Ocean Margins LINK grant NER/T/S/ 2000/0106 and NER/M/S/2000/00264, and cosponsored by ConocoPhillips, BHP Billiton, and Shell. The authors wish to thank Gianni Zuffa and Franco Ricci Lucchi (Bologna University) and Luca Martelli (Emilia Romagna Geological Survey) for advice initially on fieldwork in northern Italy. Bed correlations that form the basis of this study were made possible by the outstanding mapping of marker beds by the Italian Geological Surveys. We wish to thank Zoltan Sylvester for his insightful and constructive comments, and two anonymous reviewers.

## REFERENCES

- ALLEN, J.R.L., 1982, Chapter 10, Structures and sequences related to gravity-current surges, in *Sedimentary Structures: Their Character and Physical Basis*: Amsterdam, Elsevier, p. 395–431.
- AMY, L.A., AND TALLING, P.J., 2006, Anatomy of turbidites and co-genetic debrite intervals based on long distance (120 × 30 km) bed correlation, Marnoso Arenacea Formation, Northern Apennines, Italy: *Sedimentology*, v. 53, p. 161–212.
- AMY, L., TALLING, P.J., EDMONDS, V.O., SUMNER, E.J., AND LESEUER, A., 2005, An experimental investigation of sand mud suspension settling behaviour: implications for bimodal mud contents of submarine flow deposits: *Sedimentology*, v. 53, p. 1411–1434.
- BAAS, J.H., 1994, A flume study on the development and equilibrium morphology of current ripples in fine sand: *Sedimentology*, v. 41, p. 185–209.
- BAAS, J.H., BEST, J.L., AND PEAKALL, J., 2011, Depositional processes, bedform development and hybrid flows in rapidly decelerated cohesive (mud sand) sediment flows: *Sedimentology*, v. 58, p. 1953–1987.
- BAGNOLD, R.A., 1954, Experiments on a gravity-free dispersion of large solid spheres in a Newtonian fluid under shear: *Royal Society of London, Proceedings*, v. 225, p. 49–63.
- BEST, J., AND BRIDGE, J., 1992, The morphology and dynamics of low amplitude bedwaves upon upper stage plane beds and the preservation of planar laminae: *Sedimentology*, v. 39, p. 737–752.
- BIRMAN, V.K., MEIBURG, E., AND KNELLER, B., 2009, The shape of submarine levees: exponential or power law?: *Journal of Fluid Mechanics*, v. 619, p. 367–376.
- BONNECAZE, R.T., HUPPERT, H.E., AND LISTER, J.R., 1996, Patterns of sedimentation from polydisperse turbidity currents: *Royal Society of London, Proceedings*, v. 452, p. 2247–2261.
- BOUMA, A.H., 1962, *Sedimentology of Some Flysch Deposits: A Graphic Approach to Facies Interpretation* [PhD thesis]: University of Utrecht, The Netherlands, 168 p.
- CHOUX, C.M., AND DRUITT, T.H., 2002, Analogue study of particle segregation in pyroclastic density currents, with implications for the emplacement mechanisms of large ignimbrites: *Sedimentology*, v. 49, p. 907–928.
- DALL’OLIO, E., FELLETTI, F., AND MUTTONI, G., 2013, Magnetic-fabric analysis as a tool to constrain mechanisms of deep-water mudstone deposition in the Marnoso Arenacea Formation (Miocene, Italy) through magnetic fabric analysis: *Journal of Sedimentary Research*, v. 83, p. 170–182.
- DAS, H.S., IMRAN, J., PIRMEZ, C., AND MOHRIG, D., 2004, Numerical modeling of flow and bed evolution in meandering submarine channels: *Journal of Geophysical Research*, v. 109, p. 1978–2012.
- DE ROOIJ, F., AND DALZIEL, S.B., 2001, Time- and space-resolved measurements of deposition under turbidity currents, in McCaffrey, W.D., Kneller, B.C., and Peakall, J., eds., *Particulate Gravity Currents: International Association of Sedimentologists, Special Publication* v. 31, p. 82–91.
- DORRELL, R.M., HOGG, A.J., SUMNER, E.J., AND TALLING, P.J., 2011, The structure of the deposit produced by sedimentation of polydisperse suspensions: *Journal of Geophysical Research, Earth Surface*, v. 116, issue F1, p. 2003–2012.
- DYKSTRA, M., KNELLER, B., AND MILANA, J.P., 2012, Bed-thickness and grain-size trends in a small-scale proglacial channel-levee system; the Carboniferous Jejeles Formation, Western Argentina: implications for turbidity current flow processes: *Sedimentology*, v. 59, p. 605–622.
- ENOS, P., 1969, Anatomy of a flysch: *Journal of Sedimentary Petrology*, v. 39, p. 680–723.
- FALCINI, F., MARINI, M., MILLI, S., AND MOSCATELLI, M., 2009, An inverse problem to infer paleoflow conditions from turbidites: *Journal of Geophysical Research*, v. 114, p. 2156–2202.
- FELIX, M., 2001, A two-dimensional numerical model for a turbidity current, in McCaffrey, W.D., Kneller, B.C., and Peakall, J., eds., *Particulate Gravity Currents: International Association of Sedimentologists, Special Publication* v. 31, p. 71–81.
- FELIX, M., 2002, Flow structure of turbidity currents: *Sedimentology*, v. 49, p. 397–419.
- FRENZ, M., WYNN, R.B., GEORGIPOULOU, A., BENDER, V.B., HOUGH, G., MASSON, D.G., TALLING, P.J., AND CRONIN, B.T., 2008, Unraveling turbidite basin fill complexity: a case study from the Late Quaternary turbidite fill of the Agadir Basin, offshore Atlantic Morocco: *International Journal of Earth Sciences*, v. 98, p. 721–733.
- GLADSTONE, C., PHILLIPS, J.C., AND SPARKS, R.S.J., 1998, Experiments on bidisperse, constant-volume gravity currents: propagation and sediment deposition: *Sedimentology*, v. 45, p. 833–843.
- GRAY, T.E., ALEXANDER, J., AND LEEDER, M.R., 2005, Quantifying velocity and turbulence structure in depositing sustained turbidity currents across breaks in slope: *Sedimentology*, v. 52, p. 467–488.
- HARMS, J.C., AND FAHNESTOCK, R.K., 1965, Stratification, bed forms, and flow phenomenon (with examples from the Rio Grande), in Middleton, G.V., ed., *Primary Sedimentary Structures and Their Hydrodynamic Interpretation: SEPM, Special Publication*, v. 12, p. 84–116.
- HARRIS, T.C., HOGG, A.J., AND HUPPERT, H.E., 2002, Polydisperse particle driven gravity currents: *Journal of Fluid Mechanics*, v. 472, p. 333–371.
- HAUGHTON, P.D.W., BARKER, S.P., AND MCCAFFREY, W.D., 2003, “Linked” debrites in sand rich turbidite systems: origin and significance: *Sedimentology*, v. 50, p. 459–482.
- HAUGHTON, P.D.W., DAVIS, C., MCCAFFREY, W., AND BARKER, S.P., 2009, Hybrid sediment gravity flow deposits: classification, origin and significance, in Amy, L.A., McCaffrey, W.B., and Talling, P.J., eds., *Hybrid and Transitional Submarine Flows: Marine and Petroleum Geology*, v. 26, p. 1900–1918.
- HISCOTT, R.N., 1994, Traction-carpet stratification in turbidites: Fact or fiction?: *Journal of Sedimentary Research*, v. 64, p. 204–208.
- HISCOTT, R.N., AND MIDDLETON, G.V., 1979, Depositional mechanics of the thick-bedded sandstones at the base of a submarine slope, Tourelle Formation (Lower Ordovician), Quebec, Canada, in Doyle, L.J., and Pilkey, O.H., eds., *Geology of Continental Slopes: SEPM, Special Publication*, v. 27, p. 307–326.
- HISCOTT, R.N., AND MIDDLETON, G.V., 1980, Fabric of coarse deep-water sandstones, Tourelle Formation, Quebec, Canada: *Journal of Sedimentary Petrology*, v. 50, p. 703–722.
- KANE, I.A., KNELLER, B.C., DYKSTRA, M., KASSEM, A., AND MCCAFFREY, W.D., 2007, Anatomy of a submarine channel levee: an example from Upper Cretaceous slope sediments, Rosario Formation, Baja California, Mexico: *Marine and Petroleum Geology*, v. 24, p. 540–563.
- KANE, I.A., MCCAFFREY, W.D., PEAKALL, J., AND KNELLER, B.C., 2010, Submarine channel-levee shape and sediment waves from physical experiments: *Sedimentary Geology*, v. 223, p. 75–85.
- KYNCH, G.J., 1952, A theory of sedimentation: *Faraday Society Transactions*, v. 48, p. 166–176.

- KUBO, Y., 2004, Experimental and numerical study of topographic effects on deposition from two-dimensional, particle-driven density currents: *Sedimentary Geology*, v. 164, p. 311–326.
- KUENEN, P.H., 1966, Experimental turbidite lamination in a circular flume: *Journal of Geology*, v. 74, p. 523–545.
- KUENEN, P.H., AND SENGUPTA, S., 1970, Experimental marine suspension currents, competency and capacity: *Geology in Mijnbouw*, v. 49, p. 89–118.
- JOHNSON, C.G., AND HOGG, A.J., 2013, Entraining gravity currents: *Journal of Fluid Mechanics*, v. 731, p. 477–508.
- LECLAIR, S.F., AND ARNOTT, R.W.C., 2005, Parallel lamination formed by high-density turbidity currents: *Journal of Sedimentary Research*, v. 75, p. 1–5.
- LOWE, D.R., 1982, Sediment gravity flows 2. Depositional models with special reference to the deposits of high-density turbidity currents: *Journal of Sedimentary Petrology*, v. 52, p. 279–298.
- MCDONALD, H.A., WYNN, R.B., HUVENNE, V.A.I., PEAKALL, J., MASSON, D.G., WEAVER, P.P.E., AND MCPHAIL, S.D., 2011, New insights into the morphology, fill, and remarkable longevity (> 0.2 m.y.) of modern deep-water erosional scours along the northeast Atlantic margin: *Geosphere*, v. 7, p. 845–867.
- MUTTI, E., 1992, Turbidite Sandstones: Istituto di Geologia Università di Parma and Azienda Generale Italiana Petroli, 275 p.
- MUZZI MAGALHAES, P., AND TINTERI R., 2010, Stratigraphy and depositional setting of slurry and contained (reflected) beds in the Marnoso arenacea Formation (Langhian–Serravallian) Northern Apennines, Italy: *Sedimentology*, v. 57, p. 1685–1720.
- NAKAJIMA, T., AND KNELLER, B.C., 2011, Quantitative analysis of the geometry of submarine levees [abstract]: Geological Society of London, Internal Architecture, Bedforms and Geometry of Turbidite Channels Conference.
- PARKER, G., FUKUSHIMA, Y., AND PANTIN, H.M., 1986, Self-accelerating turbidity currents: *Journal of Fluid Mechanics*, v. 171, p. 145–181.
- PIPER, D.J.W., 1978, Turbidite muds and silts on deepsea fans and abyssal plains, in Stanley, D.J., and Kelling, G., eds., *Sedimentation in Submarine Canyons, Fans and Trenches*: Stroudsburg, Pennsylvania, Dowden, Hutchinson and Ross, p. 163–176.
- PUIG, P., PALANQUES, A., AND CANALS, M., 2014, Contemporary sediment-transport processes in submarine canyons: *Annual Review of Marine Science*, v. 6, p. 53–77.
- RICCI LUCCHI, F., AND VALMORI, E., 1980, Basin-wide turbidites in a Miocene, over-supplied deep-sea plain: a geometrical analysis: *Sedimentology*, v. 27, p. 241–270.
- RICHARDSON, J.F., AND ZAKI, W.N., 1954, The sedimentation of a suspension of uniform spheres under conditions of viscous flow: *Journal of Chemical Engineering Science*, v. 3, p. 65–73.
- SALAHELDIN, T.M., IMRAN, J., CHAUDHRY, M.H., AND REED, C., 2000, Role of fine grained sediment in turbidity current flow dynamics and resulting deposits: *Marine Geology*, v. 171, p. 21–38.
- SIMONS, D.B., RICHARDSON, E.V., AND NORDIN, C.F., 1965, Sedimentary structures formed by flow in alluvial channels, in Middleton, G.V., ed., *Primary Sedimentary Structures and their Hydrodynamic Interpretation*: SEPM, Special Publication 12, p. 34–53.
- SKENE, K.I., AND PIPER, D.J.W., 2005, Late Cenozoic evolution of Laurentian Fan: development of a glacially-fed submarine fan: *Marine Geology*, v. 27, p. 67–92.
- SKENE, K.I., PIPER, D.J.W., AND HILL, P.S., 2002, Quantitative analysis of variations in depositional sequence thickness from submarine channel levees: *Sedimentology*, v. 49, p. 1411–1430.
- SOUTHARD, J.B., 1991, Experimental determination of bed-form stability: *Annual Review of Earth and Planetary Sciences*, v. 19, p. 423–455.
- STEVENSON, C.J., TALLING, P.J., WYNN, R.B., MASSON, D.G., HUNT, J.E., FRENZ, M., AKHMETZHANOV, A., AND CRONIN, B.T., 2013, The flows that left no trace: very large-volume turbidity currents that bypassed sediment through submarine channels without eroding the seafloor: *Marine and Petroleum Geology*, v. 41, p. 186–205.
- SUMNER, E.J., AMY, L.A., AND TALLING, P.J., 2008, Deposit structure and processes of sand deposition from decelerating sediment suspensions: *Journal of Sedimentary Research*, v. 78, p. 529–547.
- SUMNER, E.J., TALLING, P.J., AND AMY, L.A., 2009, Deposits of flows transitional between turbidity current and debris flow: *Geology*, v. 37, p. 991–994.
- SUMNER, E.J., TALLING, P.J., AMY, L.A., WYNN, R.B., STEVENSON, C.J., AND FRENZ, M., 2012, Facies architecture of individual basin-plain turbidites: comparison to existing models and implications for flow processes: *Sedimentology*, v. 59, p. 1850–1887.
- TALLING, P.J., 2001, On the frequency distribution of turbidite thickness: *Sedimentology*, v. 48, p. 1297–1331.
- TALLING P.J., 2014, On the triggers, resulting flow types and frequency of subaqueous sediment density flows in different settings: *Marine Geology*, v. 352, p. 155–182.
- TALLING, P.J., AMY, L.A., WYNN, R.B., PEAKALL, J., AND ROBINSON, M., 2004, Beds comprising debrite sandwiched within co-genetic turbidite: origin and widespread occurrence in distal depositional environments: *Sedimentology*, v. 51, p. 163–194.
- TALLING, P.J., AMY, L.A., WYNN, R.B., BLACKBOURN, G., AND GIBSON, O., 2007a, Turbidity current evolution deduced from extensive thin turbidites: Marnoso Arenacea Formation (Miocene), Italian Apennines: *Journal of Sedimentary Research*, v. 77, p. 172–196.
- TALLING, P.J., AMY, L.A., AND WYNN, R.B., 2007b, New insights into the evolution of large volume turbidity currents: comparison of turbidite shape and previous modelling results: *Sedimentology*, v. 54, p. 737–769.
- TALLING, P.J., WYNN, R.B., MASSON, D.G., FRENZ, M., CRONIN, B.T., SCHIEBEL, R., AKHMETZHANOV, A.M., DALLMEIER-TIENEN, S., BENETTI, S., WEAVER, P.P.E., GEORGIPOULOU, A., ZUHLSDORFF, C., AND AMY, L.A., 2007c, Onset of submarine debris flow deposition far from original giant landslide: *Nature*, v. 450, p. 541–544.
- TALLING, P.J., WYNN, R.B., SCHMIDT, D.N., RIXON, R., SUMNER, E., AND AMY, L.A., 2010, How did thin submarine debris flows carry boulder-sized intraclasts for remarkable distances across low gradients to the far reaches of the Mississippi fan?: *Journal of Sedimentary Research*, v. 80, p. 829–851.
- TALLING, P.J., MASSON, D.G., SUMNER, E.J., AND MALGESINI, G., 2012, Subaqueous sediment density flows: depositional processes and deposit types: *Sedimentology*, v. 59, p. 1937–2003.
- TALLING, P.J., MALGESINI, G., AND FELLETTI, F., 2013a, Can liquefied (debris) flows deposit clean sandstone over large areas of sea floor? Field evidence from the Marnoso-arenacea Formation, Italian Apennines: *Sedimentology*, v. 60, p. 720–762.
- TALLING, P.J., MALGESINI, G., SUMNER, E.J., AMY, L.A., FELLETTI, F., BLACKBOURN, G., NUTT, C., WILCOX, C., HARDING, I.C., AND AKBARI, S., 2013b, Planform geometry, stacking pattern, and extrabasinal origin of low-strength and higher-strength cohesive debris flow deposits in the Marnoso arenacea Formation: *Geosphere*, v. 9, p. 460–488.
- TALLING, P.J., PAULL, C.K., AND PIPER, D.J.W., 2014, How are subaqueous sediment density flows triggered, what is their internal structure and how does it evolve? Direct observations from monitoring of active flows: *Earth Science Reviews*, v. 125, p. 244–287.
- TINTERI, R., DRAGO, M., CONSONNI, A., DAVOLI, G., AND MUTTI, E., 2003, Modelling subaqueous bipartite sediment gravity flows on the basis of outcrop constraints: first results: *Marine and Petroleum Geology*, v. 20, p. 911–933.
- WOODS, A., BURSİK, M., AND KURBATOV, A.V., 1998, The interaction of ash flows with ridges: *Bulletin of Volcanology*, v. 60, p. 38–51.
- WYNN, R.B., WEAVER, P.P.E., MASSON, D.G., AND STOWE, D.A.V., 2002, Turbidite depositional architecture across three inter-connected deep-water basins on the Northwest African Margin: *Sedimentology*, v. 49, p. 669–695.
- WYNN, R.B., TALLING, P.J., MASSON, D.G., STEVENSON, C.J., CRONIN, B.T., AND LE BAS, T.P., 2010, Investigating the timing, processes and deposits of one of the World's largest submarine gravity flows: the “Bed 5 event” off northwest Africa, in Mosher, D.C., Shipp, R.C., Moscardelli, L., Chaytor, J.D., Baxter, C.D.P., Lee, H.J., and Urgeles, R., eds., *Submarine Mass Movements and Their Consequences*: Amsterdam, Elsevier, v. 28, p. 463–474.
- XU, J.P., 2011, Measuring currents in submarine canyons: technological and scientific progress in the past 30 years: *Geosphere*, v. 7, p. 868–876.
- ZATTIN, M., PICOTTI, V., AND ZUFFA, G.G., 2002, Fission-track reconstruction of the front of the Northern Apennine thrust wedge and overlying Ligurian Unit: *American Journal of Science*, v. 302, p. 346–379.
- ZENG, Z., AND LOWE, D.R., 1997, Numerical simulation of turbidity current flow and sedimentation: II. Results and geological applications: *Sedimentology*, v. 44, p. 85–104.

Received 17 December 2012; accepted 7 November 2014.